



**HAL**  
open science

## Numerical simulation of the Von-Kármán-Sodium dynamo experiment

C Nore, D Castanon Quiroz, L Cappanera, J.-L Guermond

► **To cite this version:**

C Nore, D Castanon Quiroz, L Cappanera, J.-L Guermond. Numerical simulation of the Von-Kármán-Sodium dynamo experiment. *Journal of Fluid Mechanics*, 2018, 854, pp.164-195. 10.1017/jfm.2018.582 . hal-01575765

**HAL Id: hal-01575765**

**<https://hal.science/hal-01575765>**

Submitted on 21 Aug 2017

**HAL** is a multi-disciplinary open access archive for the deposit and dissemination of scientific research documents, whether they are published or not. The documents may come from teaching and research institutions in France or abroad, or from public or private research centers.

L'archive ouverte pluridisciplinaire **HAL**, est destinée au dépôt et à la diffusion de documents scientifiques de niveau recherche, publiés ou non, émanant des établissements d'enseignement et de recherche français ou étrangers, des laboratoires publics ou privés.

# Numerical simulation of the Von-Kármán-Sodium dynamo experiment

C. Nore<sup>1</sup>, D. Castanon Quiroz<sup>2</sup>, L. Cappanera<sup>3</sup> and J.-L. Guermond<sup>4</sup>

<sup>1</sup>Laboratoire d'Informatique pour la Mécanique et les Sciences de l'Ingénieur, LIMSI, CNRS, Univ. Paris-Sud, Université Paris-Saclay, Bâtiment 508, rue John von Neumann, Campus Universitaire, F-91405 Orsay, France;

<sup>2</sup>BCAM - Basque Center for Applied Mathematics, Mazarredo 14 E48009 Bilbao, Basque - Country, Spain;

<sup>3</sup>Department of Computational and Applied Mathematics, Rice University 6100 Main MS-134, Houston, TX 77005, USA;

<sup>4</sup>Department of Mathematics, Texas A&M University 3368 TAMU, College Station, TX 77843-3368, USA.

(Received 21 August 2017)

1 We present hydrodynamic and magnetohydrodynamic (MHD) simulations of liquid sodium  
 2 flows in the Von-Kármán-Sodium (VKS) setup. The counter-rotating impellers made of  
 3 soft iron that were used in the successful 2006 experiment are realistically represented  
 4 by means of a pseudo-penalty method. Hydrodynamic simulations are performed at high  
 5 kinetic Reynolds numbers using a Large Eddy Simulation technique. The results compare  
 6 well with the experimental data: the flow is laminar and steady or slightly fluctuating at  
 7 small angular frequencies; small scales fill the bulk and a Kolmogorov-like spectrum is  
 8 obtained at large angular frequencies. Near the tips of the blades the flow is expelled and  
 9 takes the form of intense helical vortices. The equatorial shear layer acquires a wavy shape  
 10 due to three coherent co-rotating radial vortices as observed in hydrodynamic experi-  
 11 ments. MHD computations are performed: at fixed kinetic Reynolds number, increasing  
 12 the magnetic permeability of the impellers reduces the critical magnetic Reynolds num-  
 13 ber for dynamo action; at fixed magnetic permeability, increasing the kinetic Reynolds  
 14 number also decreases the dynamo threshold. Our results support the conjecture that the  
 15 critical magnetic Reynolds number tends to a constant as the kinetic Reynolds number  
 16 tends to infinity. The resulting dynamo is a mostly axisymmetric axial dipole with an az-  
 17 imuthal component concentrated near the impellers as observed in the VKS experiment.  
 18 A speculative mechanism for dynamo action in the VKS experiment is proposed.

## 19 1. Introduction

20 Dynamo action, i.e. the self-amplification of a magnetic field by the flow of an elec-  
 21 trically conducting fluid, is considered to be the main mechanism for the generation  
 22 of the magnetic fields of stars and planets (Moffatt (1978)). In order to gain a better  
 23 understanding of the processes at play, different experimental groups have investigated  
 24 dynamo action (Peffley et al. (2000); Nornberg et al. (2006); Frick et al. (2010); Colgate  
 25 et al. (2011)) but so far only three experiments have been succesful: Gailitis et al. (2000);  
 26 Stieglitz and Müller (2001); Monchaux et al. (2007). These three experiments were all  
 27 performed in liquid sodium. The first two experiments used optimized flows guided by  
 28 pipes that intentionally limited the influence that turbulence could have on the dynamo  
 29 process. The experimentalists found dynamo action with a magnetic field having a shape  
 30 corresponding to the one predicted by using kinematic dynamo computations based on

31 analytical flows. The third dynamo has been observed in the Von-Kármán-Sodium exper-  
 32 iment (VKS) located in Cadarache: in 2006 experimentalists observed a magnetic field  
 33 generated by a turbulent flow produced by two counter-rotating impellers in a cylindrical  
 34 vessel. It has been found that both the geometry and the material composing the im-  
 35 pellers play a crucial role on the dynamo action threshold: for example, at fixed available  
 36 mechanical power, dynamo action occurs only when at least one of the rotating impellers  
 37 is made of soft iron (Miralles et al. (2013)). When the two soft iron impellers counter-  
 38 rotate at the same angular velocity, another puzzling observation is that the generated  
 39 magnetic field is statistically steady and mainly axisymmetric with an axial dipole and  
 40 a strong azimuthal component located near the impellers (Boisson et al. (2012)). This  
 41 magnetic field could not be predicted by using simplified axisymmetric geometries and  
 42 velocity fields averaged in azimuth and time: kinematic dynamo simulations usually give  
 43 an equatorial dipole superimposed with two anti-parallel vertical magnetic structures  
 44 near the vessel axis (see *e.g.* Ravelet et al. (2005); Marié et al. (2006); Laguerre et al.  
 45 (2006); Gissinger et al. (2008); Guermond et al. (2011a)).

46 It is clear that the nature of the material composing the impellers greatly influences  
 47 the transmission conditions enforced on the magnetic field, and that the geometry of the  
 48 impellers controls the dynamics of the tip vortices generated between the blades (Ravelet  
 49 et al. (2012); Kreuzahler et al. (2014)). But a precise experimental investigation of the  
 50 influences of the material properties and the blade geometry is not feasible due to the  
 51 lack of accurate techniques such as non-intrusive gaussmeters or PIV measurements in  
 52 liquid metals. It is natural then to turn to computer simulations to gain some insight  
 53 into the VKS experiment. After more than 15 years of algorithmic and code develop-  
 54 ment in MHD, we announce in the present paper that we are now capable of simulating  
 55 a realistic three-dimensional turbulent flow of liquid sodium that generates a magnetic  
 56 field that is mainly axisymmetric and similar to the one observed in the experiment. In  
 57 addition to massive parallelism, the key algorithmic factors that lead us to this result  
 58 are the development of a robust Large Eddy Simulation technique (Guermond et al.  
 59 (2011b)) and the use of pseudo-penalty method (Pasquetti et al. (2008)) to represent re-  
 60 alistic counter-rotating impellers. Early results on the Von-Kármán-Sodium experiment  
 61 obtained by direct numerical simulations of the incompressible, fully nonlinear, magneto-  
 62 hydrodynamic equations were announced in Nore, C. et al. (2016). In the present paper  
 63 we go far beyond the range of kinetic Reynolds numbers attained in the above reference.  
 64 Our main result is that the critical magnetic Reynolds number decreases as the kinetic  
 65 Reynolds number increases and this number seems to converge to a constant in the  
 66 vanishing viscosity limit. We also confirm that, everything else being fixed, the critical  
 67 magnetic Reynolds decreases as the magnetic permeability of the impellers increases.

68 The paper is organized as follows. The setup of the 2006 VKS2 experiment together  
 69 with the relevant parameters is shortly presented in section 2. The governing equa-  
 70 tions and the numerical methods that are used to solve them are also briefly described.  
 71 Section 3 presents hydrodynamical simulations performed for a large range of kinetic  
 72 Reynolds numbers. Dynamo action is studied in section 4. The impact of the relative  
 73 magnetic permeability of the impellers and of the boundary conditions is studied. The  
 74 dynamo threshold is determined for a large range of kinetic Reynolds numbers; it de-  
 75 creases as the kinetic Reynolds number increases and it seems to reach an asymptotic  
 76 value in the vanishing viscosity limit. The structure of the generated magnetic field shows  
 77 a striking similarity with the one observed in the VKS2 experiment in all of the cases  
 78 investigated. Key ingredients for dynamo action in the VKS2 setup are identified in sec-  
 79 tion 5. It is shown in particular in this section that kinematic dynamo computations  
 80 using the time averaged velocity field computed at high fluid Reynolds number give a

81 non-axisymmetric magnetic field similar to the one obtained from simplified time aver-  
 82 aged and azimuthally averaged velocity field, but this dynamo is very different from the  
 83 one observed in VKS2 experiment. Concluding remarks are reported in section 6 and a  
 84 tentative scenario is proposed.

## 85 2. Technical preliminaries

86 In the present paper we simulate numerically the VKS2 experiment with the flow driven  
 87 by the TM73 impellers (for Turbine Métallique, meaning Metal Impeller in French) (see  
 88 figure 2 and Monchaux et al. (2007)). We begin by describing the geometry. Then we  
 89 present the governing equations and the algorithms that are used in our MHD code (Guer-  
 90 mond et al. (2007, 2009, 2011a)).

### 91 2.1. Experimental setup and data

92 The VKS2 setup described in Monchaux et al. (2007) uses two concentric cylindrical  
 93 containers: the first one has a very small thickness and is of radius  $R_{\text{cyl}} = 206$  mm;  
 94 the second one is thick and made of copper, its inner radius is  $R_{\text{in}} = 289$  mm and its  
 95 outer radius is  $R_{\text{out}} = 330$  mm. Both containers have a total height  $H = 412$  mm. The  
 96 impellers are located at the two extremities of the inner container. There is some fluid  
 97 behind the impellers in the experiment, but in the present simulations we neglect this  
 98 fluid layer. The impellers are composed of two disks each supporting 8 blades. The disks  
 99 have radius  $R_b = 155$  mm and are 20 mm thick. The blades have height 41 mm, thickness  
 100 5 mm, and the angle of curvature is equal to  $24^\circ$ . The distance between the inner faces  
 101 of the disks is set to 370 mm so that the aspect ratio of the cylindrical fluid domain is  
 102  $370/206 = 1.8$ . The fluid contained in the inner vessel is pushed by the convex side of the  
 103 blades (called the unscoping sense of rotation or (+) sense). A schematic representation  
 104 of the experimental setup is shown in figure 1 using  $R_{\text{cyl}}$  as reference lengthscale.

105 The vessel contains about 150 liters of liquid sodium heated at  $120^\circ\text{C}$ . The kine-  
 106 matic viscosity is  $\nu = 6.78 \times 10^{-7} \text{m}^2 \text{s}^{-1}$ , the density is  $\rho = 932 \text{kgm}^{-3}$  and the electrical  
 107 conductivity is  $\sigma = 9.6 \times 10^6 \text{S m}^{-1}$ . The corresponding magnetic Prandtl number is  
 108  $P_m = \mu_0 \sigma \nu = 0.82 \times 10^{-5}$ . The impellers counter-rotate at a frequency  $f$ , the experimen-  
 109 tal range of frequencies necessary for observing dynamo action is  $16 \text{Hz} \leq f \leq 22 \text{Hz}$ ,  
 110 leading to kinetic Reynolds numbers in the range  $6.3 \times 10^6 \leq Re = \frac{2\pi f R_{\text{cyl}}^2}{\nu} \leq 8.7 \times 10^6$   
 111 and magnetic Reynolds numbers in the range  $52 \leq R_m^c = \mu_0 \sigma 2\pi f R_{\text{cyl}}^2 \leq 71$ .

112 At maximum available mechanical power, dynamo has been observed with soft iron  
 113 impellers (made of ferromagnetic material of relative magnetic permeability of the order  
 114 of 50, Verhille et al. (2010)) but not with stainless steel ones (Miralles et al. (2013)).

### 115 2.2. SFEMaNS

116 To investigate the hydrodynamic and magnetohydrodynamic regimes of the above ex-  
 117 perimental setup, we use a MHD code called SFEMaNS. This code uses a hybrid spatial  
 118 discretization combining spectral and finite elements. In a nutshell we use a Fourier  
 119 decomposition in the azimuthal direction and the continuous Hood-Taylor Lagrange el-  
 120 ements  $\mathbb{P}_1\text{-}\mathbb{P}_2$  for the pressure and velocity fields in the meridian section. Modulo the  
 121 computations of nonlinear terms with FFT, the linear problems for each Fourier mode  
 122 in the meridian section are uncoupled and are thereby easily parallelized by using MPI.  
 123 The solution of the linear problems in the meridian section is further parallelized by  
 124 using METIS (Karypis and Kumar (1998)) for the domain decomposition, and PETSc  
 125 (Portable, Extensible Toolkit for Scientific Computation, Balay et al. (2014)) for the lin-  
 126 ear algebra. For the magnetic part, the algorithm solves the problem using the magnetic

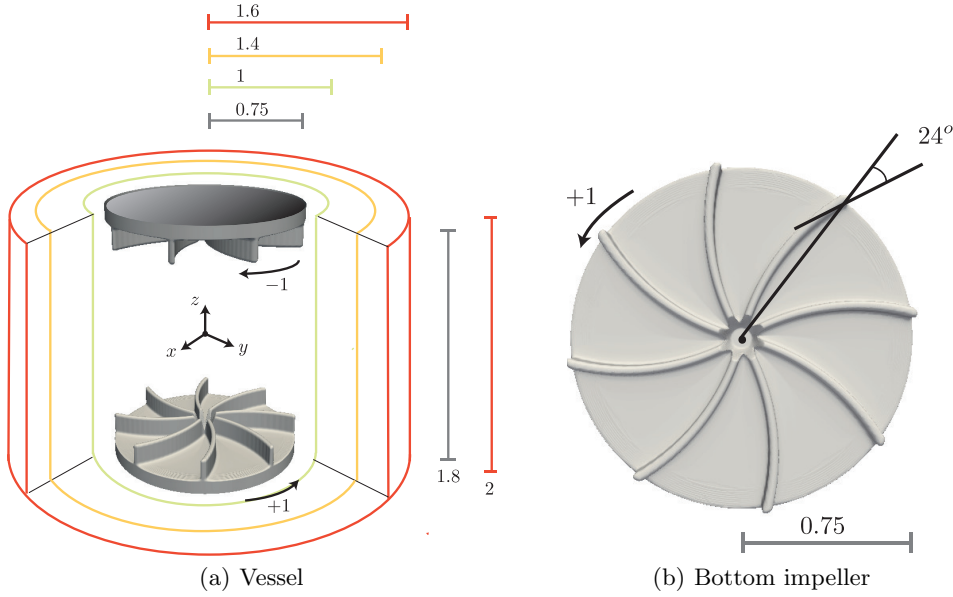


FIGURE 1. Schematic of the VKS2 experimental device of Monchaux et al. (2007) in non-dimensional units. The impellers counter-rotate as indicated in (a) and are fitted with 8 curved blades (see b).

127 induction,  $\mathbf{B}$ , in the conducting region (after standard elimination of the electric field)  
 128 and the scalar magnetic potential in the insulating exterior. The fields in each region are  
 129 approximated by using  $H^1$ -conforming Lagrange elements with a penalty technique to  
 130 control the divergence of  $\mathbf{B}$  in a negative Sobolev norm that guarantees convergence un-  
 131 der minimal regularity (see details in Bonito and Guermond (2011), Giesecke et al. (2010,  
 132 §3.2), Bonito et al. (2013)). The coupling between conducting and insulating media is  
 133 done by using an interior penalty method. SFEMaNS has been thoroughly validated on  
 134 numerous manufactured solutions and against other MHD codes (see e.g. Guermond et al.  
 135 (2009); Giesecke et al. (2012); Nore et al. (2016)). The reader who is familiar with the  
 136 numerical details or is not interested in such details is now invited to jump to section 3.

### 137 2.3. Governing equations

Let us now go into some details about the equations that are actually solved in SFEMaNS.  
 The MHD equations are solved in non-dimensional form as follows:

$$\partial_t \mathbf{u} = -(\nabla \times \mathbf{u}) \times \mathbf{u} + \frac{1}{Re} \Delta \mathbf{u} - \nabla p + \mathbf{f}, \quad (2.1a)$$

$$\partial_t \mathbf{B} = \nabla \times (\mathbf{u} \times \mathbf{B}) - \frac{1}{R_m} \nabla \times \left( \frac{1}{\sigma_r} \nabla \times \left( \frac{1}{\mu_r} \mathbf{B} \right) \right), \quad (2.1b)$$

$$\nabla \cdot \mathbf{u} = 0, \quad (2.1c)$$

$$\nabla \cdot \mathbf{B} = 0, \quad (2.1d)$$

138 where  $\mathbf{u}$  is the velocity field,  $\mathbf{B}$  the magnetic induction field (with the magnetic field  $\mathbf{H} =$   
 139  $\mathbf{B}/\mu_0\mu_r$ ),  $p$  the pressure field, and  $\sigma_r, \mu_r$  are the relative conductivity and permeability  
 140 of the various materials in presence. The Navier-Stokes and the Maxwell equations are  
 141 coupled by the Lorentz force  $\mathbf{f} = (\nabla \times \mathbf{H}) \times \mathbf{B}$ .

142 In the present situation the reference length  $L_{\text{ref}}$  is set to  $R_{\text{cyl}}$ . The computational  
 143 domain for the hydrodynamic study is  $\Omega = \{(r, \theta, z) \in [0, 1] \times [0, 2\pi) \times [-1, 1]\}$ . The  
 144 computational domain for the MHD study is the larger cylinder  $\Omega \cup \Omega_{\text{out}}$  with  $\Omega_{\text{out}} =$

145  $\{(r, \theta, z) \in [1, 1.6] \times [0, 2\pi] \times [-1, 1]\}$ . Denoting by  $\sigma_0$  the electrical conductivity of the  
 146 liquid sodium,  $\rho$  its density, and  $\mu_0$  the magnetic permeability of vacuum, the magnetic  
 147 induction is made non-dimensional by using the Alfvén scaling  $B = U\sqrt{\rho\mu_0}$ , with  $U =$   
 148  $\omega R_{\text{cyl}}$  where  $\omega$  is the angular velocity of the impellers. The two governing parameters  
 149 are  $R_{\text{m}} = \mu_0\sigma_0 R_{\text{cyl}}^2\omega$ , the magnetic Reynolds number, and  $R_{\text{e}} = R_{\text{cyl}}^2\omega/\nu$ , the kinetic  
 150 Reynolds number, with  $\nu$  the kinematic viscosity of the fluid.

151 Note that the parameters  $\sigma_r$ ,  $\mu_r$  are not constant since the walls and the impellers  
 152 are made of different materials like copper, steel and soft iron. Specifically, we take  $\sigma_r =$   
 153  $1$ ,  $\mu_r = 1$  in the region  $\{(r, \theta, z) \in [1, 1.4] \times [0, 2\pi] \times [-1, 1]\}$  to represent the lateral layer  
 154 of stagnant liquid sodium, and  $\sigma_r = 4.5$ ,  $\mu_r = 1$  in  $\{(r, \theta, z) \in [1.4, 1.6] \times [0, 2\pi] \times [-1, 1]\}$   
 155 to model the lateral copper wall. In the induction equation (2.1b) we take  $\mathbf{u}|_{\Omega_{\text{out}}} = 0$ . At  
 156 the exception of section 4.3 where we study the impact of the so-called vacuum boundary  
 157 condition, in the entire paper we impose the perfect ferromagnetic boundary condition  
 158  $\mathbf{H} \times \mathbf{n} = 0$  at the boundary of the computational domain. We shall also refer to this  
 159 condition as the pseudo-vacuum boundary condition. This boundary condition allows us  
 160 to save memory and CPU time.

#### 161 2.4. Moving domains

162 To distinguish the liquid sodium from the impellers, the cylinder  $\Omega$  is split into a solid  
 163 domain  $\Omega_{\text{solid}}(t)$  (composed of the rotating impellers) and a fluid domain  $\Omega_{\text{fluid}}(t)$ , and  
 164 we introduce the characteristic function  $\chi$  defined in cylindrical coordinates by:

$$\chi(r, \theta, z, t) = \begin{cases} 1 & \text{if } (r, \theta, z) \in \Omega_{\text{fluid}}(t) \\ 0 & \text{if } (r, \theta, z) \in \Omega_{\text{solid}}(t). \end{cases} \quad (2.2)$$

In our case  $\chi = 0$  in the impellers (see figure 1). Note that both  $\Omega_{\text{solid}}(t)$  and  $\Omega_{\text{fluid}}(t)$  are  
 time-dependent. It is not possible to find a frame of reference where these domains are  
 time-independent since the impellers move with opposite angular velocities. The ensuing  
 main difficulty is to approximate the Navier-Stokes equations in a time and  $\theta$ -dependent  
 domain and to force the velocity in the solid domain  $\Omega_{\text{solid}}(t)$  to be that of two solid bodies  
 in rotation. This is achieved by using a prediction-correction method of Guermond and  
 Shen (2004) and a pseudo-penalty technique of Pasquetti et al. (2008). Let  $\tau$  be the time  
 step and let us generically denote by  $f^n$  the approximation of  $f(n\tau)$ . The velocity is then  
 updated by using the following scheme:

$$\begin{aligned} \frac{3\mathbf{u}^{n+1}}{2\tau} - \frac{1}{R_{\text{e}}}\Delta\mathbf{u}^{n+1} &= -\nabla p^n + (1 - \chi^{n+1})\frac{3\mathbf{u}_{\text{obs}}^{n+1}}{2\tau} \\ &+ \chi^{n+1} \left( \frac{4\mathbf{u}^n - \mathbf{u}^{n-1}}{2\tau} - \nabla \left( \frac{4\psi^n - \psi^{n-1}}{3} \right) - (\nabla \times \mathbf{u}^{*,n+1}) \times \mathbf{u}^{*,n+1} + \mathbf{f}^{n+1} \right), \end{aligned} \quad (2.3)$$

165 where  $\mathbf{u}^{*,n+1} = 2\mathbf{u}^n - \mathbf{u}^{n-1}$  and, using cylindrical coordinates,  $\mathbf{u}_{\text{obs}}$  is the velocity of the  
 166 disks and blades defined for all  $n \geq 0$  by:

$$\mathbf{u}_{\text{obs}}^n(r, \theta, z) = \begin{cases} -r\mathbf{e}_\theta & \text{if } z > 0, \\ r\mathbf{e}_\theta & \text{if } z \leq 0. \end{cases} \quad (2.4)$$

167 The pressure increment  $\psi^{n+1}$  is obtained by solving the following Poisson problem:

$$\Delta\psi^{n+1} = \frac{3}{2\tau}\nabla \cdot \mathbf{u}^{n+1}. \quad (2.5)$$

168 The pressure is finally updated as follows:

$$p^{n+1} = p^n + \psi^{n+1} - \frac{1}{R_{\text{e}}}\nabla \cdot \mathbf{u}^{n+1}. \quad (2.6)$$

169 Note that the velocity and the pressure are solutions of the Navier-Stokes equations when  
 170  $\chi = 1$ , i.e., in the fluid domain  $\Omega_{\text{fluid}}(t)$ . When  $\chi = 0$ , i.e., in  $\Omega_{\text{solid}}(t)$ , the momentum  
 171 equation reduces to  $\frac{3\mathbf{u}^{n+1}}{2\tau} - \frac{1}{R_e} \Delta \mathbf{u}^{n+1} = -\nabla p^n + \frac{3\mathbf{u}_{\text{obs}}^{n+1}}{2\tau}$ ; to first order in  $\tau$ , the solution is  
 172  $\mathbf{u} = \mathbf{u}_{\text{obs}} + O\left(\frac{\tau}{R_e}\right)$ . Note that the higher the kinetic Reynolds number, the more accurate  
 173 the method. There are two situations for the initialization of the above algorithm. Either  
 174 we start from rest, and in this case all the quantities required at  $n = 0$  are set to zero,  
 175 or we restart from a previous computation, and in this case all the quantities required to  
 176 restart are taken from the previous computation.

177 The second difficulty we face is that the material properties in the computational frame  
 178 depend on the azimuthal angle and time due to the presence of the rotating blades. This  
 179 is not a serious issue for the conductivity  $\sigma_r$  since the conductivity of the impellers  
 180 and the liquid sodium are not very different; for the sake of simplicity we take  $\sigma_r = 1$   
 181 in the impellers and in the liquid sodium. But to account for the heterogenities of the  
 182 magnetic permeability, we allow  $\mu_r$  to depend on all the space and time variables, i.e.,  
 183  $\mu_r = \mu_r(r, \theta, z, t)$ . More precisely, letting  $\mu_r^{\text{imp}}$  be the relative permeability of the impellers  
 184 and recalling that  $\mu_r = 1$  in the liquid sodium, we set

$$\mu_r(r, \theta, z, t) = \chi(r, \theta, z, t) + (1 - \chi(r, \theta, z, t))\mu_r^{\text{imp}}. \quad (2.7)$$

In order to make the linear algebra in the induction equation time-independent, and to  
 avoid the nonlinearity in  $\theta$  induced by the product  $\frac{1}{\mu_r} \mathbf{B}$ , we split the diffusion term by set-  
 ting  $\frac{\mathbf{B}}{\mu_r} = \frac{\mathbf{B}}{\widetilde{\mu}_r} + \left(\frac{\mathbf{B}}{\mu_r} - \frac{\mathbf{B}}{\widetilde{\mu}_r}\right)$ , where  $\widetilde{\mu}_r(r, z)$  is defined by  $\widetilde{\mu}_r(r, z) := \min_{0 \leq \theta < 2\pi} \mu_r(r, \theta, z, t)$ .  
 The first part of the decomposition,  $\frac{\mathbf{B}}{\widetilde{\mu}_r}$ , is made implicit while the second part,  $\left(\frac{\mathbf{B}}{\mu_r} - \frac{\mathbf{B}}{\widetilde{\mu}_r}\right)$ ,  
 is made explicit by using  $\mathbf{B}^{*,n+1} = 2\mathbf{B}^n - \mathbf{B}^{n-1}$  and  $\mu_r = \mu_r^{n+1}$ . The magnetic induction  
 field is therefore updated as follows:

$$\begin{aligned} \frac{3\mathbf{B}^{n+1}}{2\tau} + \frac{1}{R_m} \nabla \times \left( \frac{1}{\sigma_r} \nabla \times \left( \frac{\mathbf{B}^{n+1}}{\widetilde{\mu}_r} \right) \right) &= \frac{4\mathbf{B}^n - \mathbf{B}^{n-1}}{2\tau} \\ &+ \nabla \times (\mathbf{u}^{n+1} \times \mathbf{B}^{*,n+1}) - \frac{1}{R_m} \nabla \times \left( \frac{1}{\sigma_r} \nabla \times \left( \mathbf{B}^{*,n+1} \left( \frac{1}{\mu_r} - \frac{1}{\widetilde{\mu}_r} \right) \right) \right). \end{aligned} \quad (2.8)$$

185 The function  $\widetilde{\mu}_r$  being independent of the azimuth, implicit FFT convolutions are com-  
 186 pletely avoided. Note also that for each Fourier mode, the linear problem in (2.8) is de-  
 187 coupled from the other Fourier modes. The scheme (2.8) is stable, owing to the condition  
 188  $\widetilde{\mu}_r \leq \mu_r$ , and it can be shown to be second-order accurate in time, see Castanon Quiroz  
 189 (2015) for details. Finally, the solenoidal constraint (2.1d) is enforced as in Guermond  
 190 et al. (2011a).

### 191 2.5. Entropy viscosity stabilization

192 When  $R_e$  is moderate, it is possible to resolve all the scales by refining the grid and  
 193 by enriching the Fourier space, i.e., it is possible to perform Direct Numerical Simula-  
 194 tions (DNS, see table 1), but, given that computer resources are finite, this is no longer  
 195 feasible when  $R_e$  becomes large. More specifically, given a fixed computational budget,  
 196 large gradients induced by the turbulence cascade can no longer be correctly represented  
 197 numerically for Reynolds numbers beyond a few thousands. The energy that should have  
 198 been dissipated at the Kolmogorov scale accumulates at the grid scale. A stabilization  
 199 method that handles this problem has been implemented in SFEMaNS. This method,  
 200 called entropy viscosity and denoted LES in table 1, was developed in Guermond et al.  
 201 (2011b) and Guermond et al. (2011c). It consists of adding a local artificial viscosity  
 202 made proportional to the residual of the kinetic energy balance. This artificial viscosity

$R_e$	$1.5 \times 10^3$	$1.5 \times 10^3$	$1.5 \times 10^3$	$2.5 \times 10^3$	$10^4$	$10^5$
$R_m$	[50, 300]	[50, 300]	[50, 300]	[50, 150]	[50, 150]	[50, 100]
Model	DNS	–	–	LES	–	–
$\mu_r^{\text{imp}}$	1	5	50	50	50	50
$\tau$	$1.25 \times 10^{-3}$	$1.25 \times 10^{-3}$	$10^{-3}$	$10^{-3}$	$1.25 \times 10^{-3}$	$1.25 \times 10^{-3}$
$h_{\min}$	$2.5 \times 10^{-3}$	–	–	$5 \times 10^{-3}$	–	–
$h_{\max}$	$10^{-2}$	–	–	–	–	–
modes	128	128	128	144	168 or 256	168 or 256
nprocs	64	64	192	360	336 or 512	336 or 512

TABLE 1. Numerical parameters for the MHD computations: kinetic Reynolds number  $R_e$ , magnetic Reynolds number  $R_m$ , numerical model DNS or LES, maximum relative magnetic permeability for impellers  $\mu_r^{\text{imp}}$ , timestep, mesh size in the blade region  $h_{\min}$ , mesh size at the outer boundary  $h_{\max}$  (the meridian mesh is non-uniform), number of real Fourier modes, number of processors.

is added on the right-hand side of (2.1a) in the form  $\nabla \cdot (\nu_E \nabla \mathbf{u})$ . This induces a nonlinear diffusion proportional to the local energy imbalance that in turn allows the unresolved scales to be better accounted for.

Let us now give some technical details on the computation of the entropy viscosity. We consider a mesh  $\mathcal{K}_h$  of the computational domain composed of a collection of cells  $K$  with local mesh-size  $h_K$ . Assuming that  $n \geq 2$  (or  $\mathbf{u}^{-2}$ ,  $\mathbf{u}^{-1}$ , and  $p^{-1}$  have been initialized appropriately), we define the residual of the momentum equation as follows:

$$\text{Res}_{\text{NS}}^n = \frac{\mathbf{u}^n - \mathbf{u}^{n-2}}{2\tau} + (\mathbf{u}^{n-1} \cdot \nabla) \mathbf{u}^{n-1} - \frac{1}{R_e} \Delta \mathbf{u}^{n-1} + \nabla p^{n-1} - \mathbf{f}^{n-1}. \quad (2.9)$$

This residual is computed at each time step and over every mesh cell. The local artificial viscosity is defined on each cell  $K$  by:

$$\nu_{R|K}^n = \frac{h_K^2 \|\text{Res}_{\text{NS}}^n \cdot \mathbf{u}^n\|_{\mathbf{L}^\infty(D_K)}}{\|\mathbf{u}^n\|_{\mathbf{L}^\infty(D_K)}^2}. \quad (2.10)$$

where  $D_K$  is the patch composed of the cells sharing one face with the cell  $K$ . The quantity  $\nu_{R|K}^n$  is expected to be as small as the consistency error in smooth regions and to be large in the regions where the Navier-Stokes equations are not resolved well. To be able to run with CFL numbers of order  $\mathcal{O}(1)$ , we finally define the entropy viscosity as follows:

$$\nu_{E|K}^n = \min \left( c_{\max} h_K \|\mathbf{u}^n\|_{\mathbf{L}^\infty(D_K)}, c_e \nu_{R|K}^n \right), \quad (2.11)$$

where  $c_{\max} = \frac{1}{8}$  (for  $\mathbb{P}_2$  approximation on the velocity) and  $c_e$  is a tunable constant  $\mathcal{O}(1)$ . Thus defined, and given that we use  $\mathbb{P}_2$  polynomials to approximate the velocity, the entropy viscosity scales like  $\mathcal{O}(h_K^3)$  in smooth regions and scales like  $\mathcal{O}(h_K)$  in regions with very large gradients.

No artificial viscosity is added in the induction equation (2.1b) because the magnetic Reynolds number  $R_m$  is always far smaller than the kinetic Reynolds number, therefore the magnetic field is always correctly represented by the finite element mesh.

## 2.6. Summary of the numerical parameters

The numerical parameters that have been used in the various simulations reported in the paper are listed in table 1. The spatial resolution of a typical DNS run in the meridian plane is  $h_{\min} = 2.5 \times 10^{-3}$  in the blade region and  $h_{\max} = 10^{-2}$  close to the outer



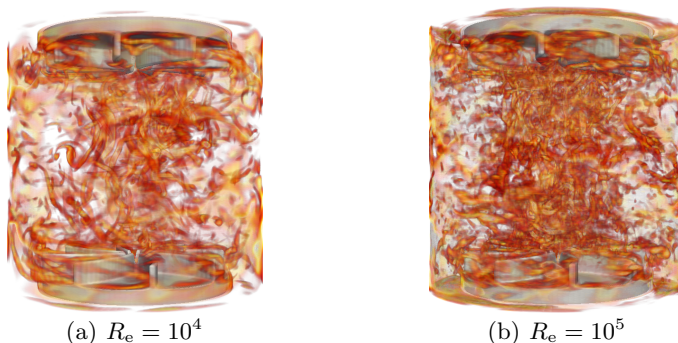


FIGURE 2. Navier-Stokes simulations in the TM73 VKS2 configuration in the cylinder of radius  $r = 1$ : (a) at  $Re = 10^4$ , partial scale for the vorticity field  $\nabla \times \mathbf{u}$  (between 10 and 25 for a total scale between 0 and 56) and (b) at  $Re = 10^5$  partial scale for the vorticity field  $\nabla \times \mathbf{u}$  (between 10 and 25 for a total scale between 0 and 99). Impellers are represented in light grey.

217 boundary and slightly coarser for a typical LES run. Between 128 to 256 real Fourier  
 218 modes are used. The parallelization is done with one complex Fourier mode per proces-  
 219 sor, and the meridian plane is further divided among the processors by using a domain  
 220 decomposition technique, the graph partitioning being done by METIS. The linear algebra  
 221 in the meridian section is handled by PETSc and the FFTs are done with FFT3W.  
 222 One rotation period (one turn) requires between 5 to 8 wall-clock hours on a medium  
 223 capacity parallel machine called Brazos at Texas A&M University with quad core Intel  
 224 Xeon, AMD Opteron and 8-core AMD Opteron, and it takes between 2 to 4 wall-clock  
 225 hours on the cluster IBM x3750-M4 from GENCI-IDRIS. Each run does between 15 to  
 226 60 turns. The cumulated computing time for the runs presented in this article is about  
 227  $5 \times 10^5$  CPU hours on one processor.

### 228 3. Hydrodynamic study

229 We first perform hydrodynamic computations by solving the equations  $\{(2.1a)-(2.1c)\}$   
 230 with  $Re$  in the range  $\{2 \times 10^2, 5 \times 10^2, 10^3, 1.5 \times 10^3, 2.5 \times 10^2, 10^4, 10^5\}$ . We characterize the  
 231 structures of the flow through three-dimensional visualizations and by computing vari-  
 232 ous time-averaged physical quantities. The visualizations, the global quantities, and the  
 233 spatial spectra are in agreement with the experimental observations and the Kolmogorov  
 234 scenario. All the simulations done at  $Re = 2500$  and beyond have been done with the  
 235 entropy viscosity technique presented previously.

#### 236 3.1. Turbulent flow at high Reynolds numbers

237 We start by investigating the qualitative behavior of the flow at high Reynolds numbers.  
 238 Figure 2 shows instantaneous vorticity fields at  $Re = 10^4$  and  $Re = 10^5$  characterized by  
 239 small-scale structures with a clustering near the symmetry axis. The numerous vorticity  
 240 tubes are characteristic of fully developed turbulence. Elongated vortical structures are  
 241 attached to the concave side of the impeller blades.

242 We show in figure 3 one snapshot of the velocity field computed at  $Re = 10^5$ . The  
 243 flow is clearly turbulent as small scales have invaded the entire fluid domain. In the  $yOz$   
 244 plane the instantaneous velocity components  $\{u_x, u_y\}$  show ejection motions near the  
 245 tip of the impellers. Close to the symmetry axis, the  $u_z$ -component shows strong axial  
 246 motions that are oriented toward the center of the cylinder and which are characteristics  
 247 of the Ekman suction induced by the impellers (see figure 3 a-c). The representation of

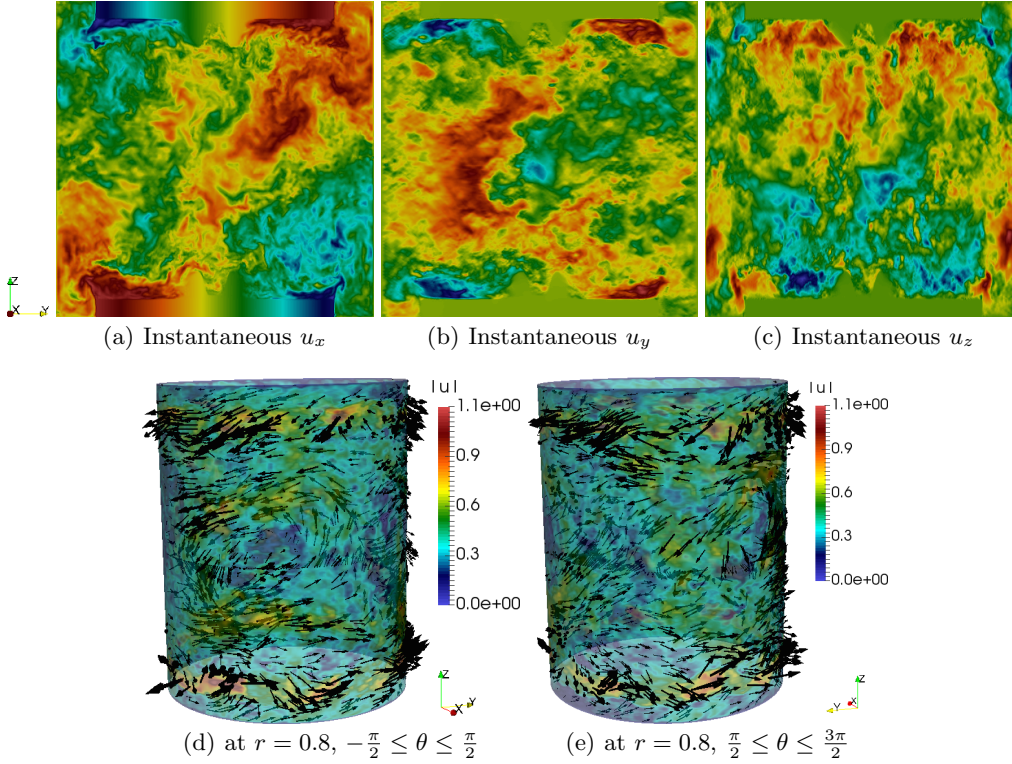


FIGURE 3. Navier-Stokes simulations in the TM73 VKS2 configuration at  $Re = 10^5$ . Instantaneous velocity field in the plane  $yOz$  ( $-1 \leq y \leq 1$ ,  $-1 \leq z \leq 1$ ): (a)  $u_x$  (scale between  $-0.94$  (blue) and  $0.85$  (red)); (b)  $u_y$  (scale between  $-0.83$  (blue) and  $0.77$  (red)); (c)  $u_z$  (scale between  $-0.66$  (blue) and  $0.69$  (red)). Instantaneous velocity vector field on the cylindrical surface  $\{r = 0.8\}$ : (d) for  $-\frac{\pi}{2} \leq \theta \leq \frac{\pi}{2}$ ; (e) for  $\frac{\pi}{2} \leq \theta \leq \frac{3\pi}{2}$ .

248 the velocity vector field on the cylindrical surface  $\{r = 0.8\}$  reveals two counter-rotating  
 249 zonal flows at the top and bottom of the vessel which are induced by the impellers. We  
 250 also observe large scale structures in the equatorial plane where the  $\{u_\theta, u_z\}$ -components  
 251 are significantly larger than the radial component  $u_r$  (see figure 3(d-e)).

252 The overall structure is made more visible by inspecting the time-average of the velocity  
 253 field (see figure 4(a-g)). We observe two counter-rotating recirculation tori separated by  
 254 an active azimuthal shear layer localized at the equator. Kinetic energy is injected by the  
 255 impellers, the flow spirals up or down along the sidewall and is driven radially inward at  
 256 mid-plane. The two resulting inward flows meet at the equator and form a shear layer  
 257 that dissipates energy. Note that the components of the time-averaged velocity shown  
 258 in figure 4(a-c) are not fully symmetric with respect to the  $Oz$  and  $Oy$  axes due to the  
 259 presence of the azimuthal Fourier mode  $m = 3$ . The spectra reported in figure 9 show  
 260 that the azimuthal Fourier mode  $m = 3$  is persistent over a wide range of Reynolds  
 261 numbers. This energy peak at  $m = 3$  corresponds to three radial co-rotating vortices  
 262 seen in figure 4(d-e). These cat's-eye structures are the manifestation of the Kelvin-  
 263 Helmholtz instability of the equatorial shear layer (Nore et al. (2003)). These vortices  
 264 are localized near the equator and form a complex 3D structure inside the bulk as evidenced  
 265 in figure 4(f-g). The cat's-eye vortices have been experimentally observed by Cortet et al.  
 266 (2009) at even higher Reynolds numbers.

267 As seen in figure 5a, the global kinetic helicity  $\text{Hel}_K(t) := \int_\Omega \mathbf{u}(\mathbf{r}, t) \cdot \nabla \times \mathbf{u}(\mathbf{r}, t) d\Omega$  is

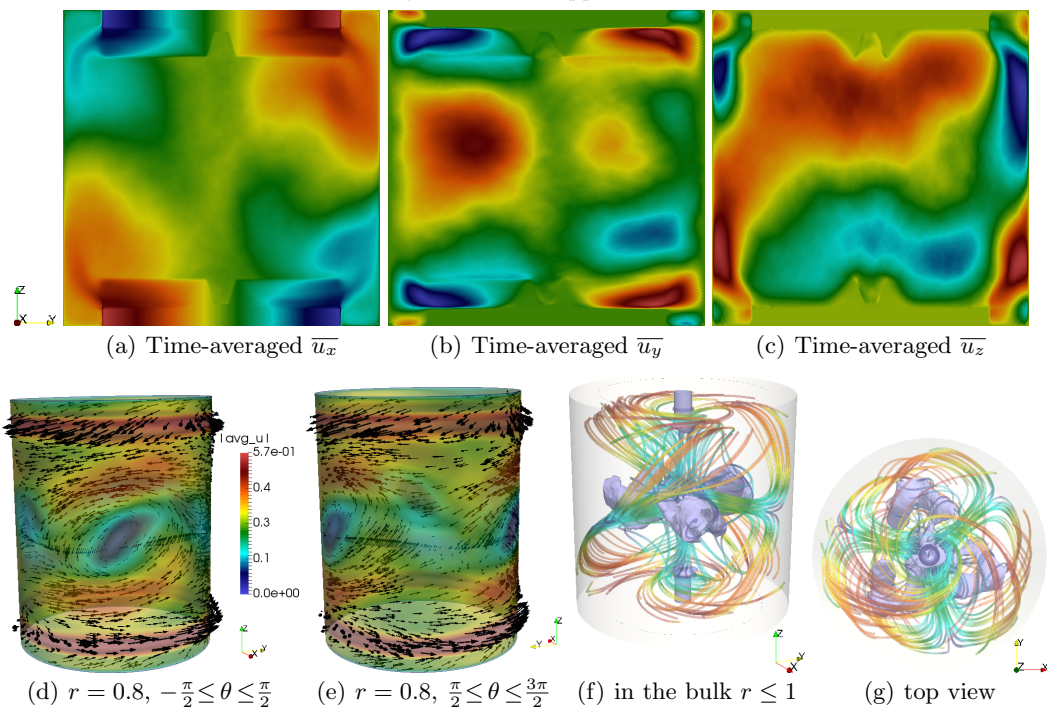


FIGURE 4. Same as figure 3 for the time-averaged velocity field. Velocity field in the plane  $yOz$  ( $-1 \leq y \leq 1, -1 \leq z \leq 1$ ): (a)  $\overline{u_x}$  (scale between  $-0.75$  (blue) and  $0.75$  (red)); (b)  $\overline{u_y}$  (scale between  $-0.34$  (blue) and  $0.39$  (red)); (c)  $\overline{u_z}$  (scale between  $-0.37$  (blue) and  $0.33$  (red)). Velocity vector field on the cylindrical surface  $\{r = 0.8\}$ : (d) for  $-\frac{\pi}{2} \leq \theta \leq \frac{\pi}{2}$ ; (e) for  $\frac{\pi}{2} \leq \theta \leq \frac{3\pi}{2}$ . Isosurface of 10% of the velocity magnitude (purple) with streamlines (colored by velocity magnitude): (f) from a perspective; (g) top view; the cylinder  $\{r = 1\}$  is in light grey.

268 negative during the entire time evolution. This is not a surprise since the Ekman suction  
 269 creates a strong vertical velocity field moving toward each impeller and the product of this  
 270 velocity field with the angular velocity of the impellers is dominantly negative. However  
 271 the spatial distribution of the instantaneous local helicity  $\mathbf{u}(\mathbf{r}, t) \cdot \nabla \times \mathbf{u}(\mathbf{r}, t)$  is complex  
 272 and exhibits fine scales (see figure 5b-c). The instantaneous maxima are always localized  
 273 near the impellers whereas the minima are dispersed over the whole fluid domain. This is  
 274 well illustrated in figure 5c where we show the helicity field of the time-averaged velocity.  
 275 As first numerically evidenced by Ravelet et al. (2012); Kreuzahler et al. (2014) and seen  
 276 in figure 2, the positive maxima are associated with the right-handed swirling vortices  
 277 attached to each blade and occupying the space between the blades. These vortices  
 278 are thought to be a key ingredient of the dynamo mechanism (Laguerre et al. (2008);  
 279 Gissinger (2009); Varela et al. (2015)).

280

### 3.2. Global quantities

281 We now make quantitative diagnostics to get a better understanding of the dynamics.  
 282 Given a finite time series  $f^1, \dots, f^q$ , we define the time average  $\overline{f}$  as follows:

$$\overline{f} := \frac{1}{q} \sum_{1 \leq n \leq q} f^n. \quad (3.1)$$

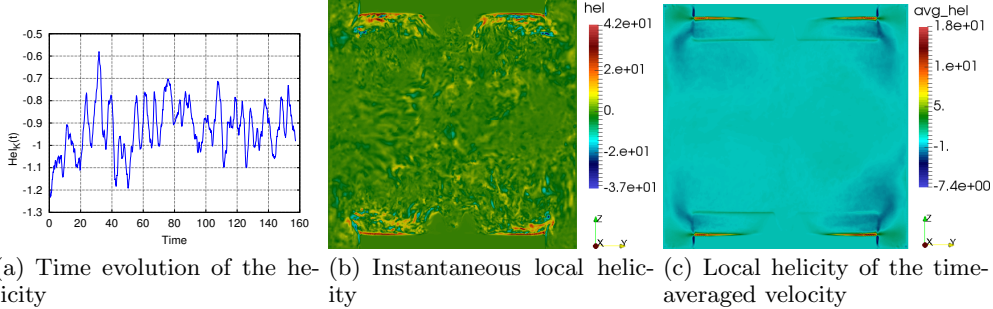


FIGURE 5. Navier-Stokes simulations in the TM73 VKS2 configuration at  $Re = 10^5$ : (a) time evolution of the total helicity  $Hel_K(t)$ ; (b) instantaneous local helicity in the  $yOz$  plane at time  $t = 125$ ; (c) local helicity of the time-averaged velocity in the  $yOz$  plane.

283 The first quantities of interest are the kinetic energy  $E$ , the root mean square velocity,  
 284 and an indicator of the fluctuation level  $\delta$  defined by:

$$E(t) := \frac{1}{2} \int_{\Omega} |\mathbf{u}(\mathbf{r}, t)|^2 d\Omega, \quad U_{\text{RMS}} := \sqrt{\frac{2E}{|\Omega|}}, \quad \delta(\mathbf{u})(t) := \frac{\|\mathbf{u}\|_{L^2(\Omega)}^2}{\|\bar{\mathbf{u}}\|_{L^2(\Omega)}^2}. \quad (3.2)$$

285 We also introduce the poloidal and the toroidal components of the velocity field which  
 286 we denote by  $P(\mathbf{u})$  and  $T(\mathbf{u})$ , respectively. Using the same notation and convention as  
 287 in Ravelet (2005), we set:

$$P(\mathbf{u}) := \frac{1}{|\Omega|} \int_{\Omega} \sqrt{u_{r,0}^2 + u_{z,0}^2} d\Omega, \quad T(\mathbf{u}) := \frac{1}{|\Omega|} \int_{\Omega} |u_{\theta,0}| d\Omega, \quad \Gamma(\mathbf{u}) := \frac{P(\mathbf{u})}{T(\mathbf{u})}, \quad (3.3)$$

288 where  $u_{r,0}$ ,  $u_{\theta,0}$ , and  $u_{z,0}$  are the radial, azimuthal, and vertical components of the Fourier  
 289 mode  $m = 0$  of the velocity  $\mathbf{u}$ . We finally consider the dimensionless torque  $K_p$  defined  
 290 by:

$$K_p = \frac{1}{2} \int_{\Omega_{\text{solid}}} |(\mathbf{r} \times \mathbf{f}_s) \cdot \mathbf{e}_z| d\Omega, \quad (3.4)$$

291 where  $\mathbf{f}_s$  is the non-dimensional body force that induces the solid rotation of the impellers.  
 292 Using the notation from (2.2)–(2.4), we deduce from the expression of the discrete mo-  
 293 mentum balance (2.3) that the torque at time  $t_{n+1}$  is given by

$$K_p = \frac{1}{2} \int_{\Omega} r(1 - \chi) \text{sign}(z) \frac{1}{2\tau} (4\mathbf{u}^n - \mathbf{u}^{n-1} - 3\mathbf{u}_{\text{obs}}) \cdot \mathbf{e}_{\theta} d\Omega, \quad (3.5)$$

294 with  $\text{sign}(z)$  equal to 1 if  $z > 0$  and  $-1$  otherwise.

295 We have reported in Table 2 the quantities  $\bar{E}$ ,  $\overline{\delta(\mathbf{u})}$ ,  $\overline{P(\mathbf{u})}$ ,  $\overline{T(\mathbf{u})}$ ,  $\overline{\Gamma(\mathbf{u})}$ ,  $U_{\text{RMS}}$ , and  $\overline{K_p}$   
 296 for all the runs we have done with  $Re \in \{2 \times 10^2, 5 \times 10^2, 10^3, 1.5 \times 10^3, 2.5 \times 10^3, 10^4, 10^5\}$ .  
 297 With the exception of  $\overline{K_p}$  and  $\overline{\delta(\mathbf{u})}$ , all the quantities increase with  $Re$ . In particular the  
 298 ratio  $\overline{\Gamma}$  increases with  $Re$  and reaches the value 0.57 at  $Re = 10^5$ . Using TM73 impellers,  
 299 Ravelet et al. (2005) measured  $\overline{\Gamma} \approx 0.8$  at  $Re > 10^5$ . The ratio  $\overline{\Gamma}$  is expected to play a  
 300 major role in the generation of a magnetic field by the flow; in particular, values around  
 301 0.7 are thought to be near-optimal (see figure 5 of Ravelet et al. (2005)).

302 Upon inspection of figure 6, where we have reported the time-averaged torque as a  
 303 function of the Reynolds number, we observe that  $\overline{K_p}$  has a non-monotonic behavior  
 304 with respect to  $Re$  that is similar to the drag crisis of a sphere or a cylinder. We also  
 305 note that  $\overline{K_p}$  seems to be converging to a nonzero asymptotic limit in the vanishing  
 306 viscosity limit. Note that  $\overline{\delta(\mathbf{u})}$  has the same behavior. The behavior of  $\overline{K_p}$  and  $\overline{\delta(\mathbf{u})}$  is

---

$R_e$	$\overline{E}$	$\overline{\delta(\mathbf{u})}$	$\overline{P(\mathbf{u})}$	$\overline{T(\mathbf{u})}$	$\overline{\Gamma(\mathbf{u})}$	$U_{\text{RMS}}$	$\overline{K_p}$
$2 \times 10^2$	0.2287	1.0122	0.0753	0.1936	0.3892	0.2698	0.06311
$5 \times 10^2$	0.2983	1.0201	0.0933	0.2005	0.4653	0.3082	0.05313
$10^3$	0.3893	1.1172	0.1145	0.2460	0.4651	0.3520	0.05047
$1.5 \times 10^3$	0.4078	1.2123	0.1157	0.2263	0.5113	0.3603	0.05078
$2.5 \times 10^3$	0.4427	1.3461	0.1244	0.2193	0.5671	0.3754	0.05198
$10^4$	0.4908	1.5429	0.1313	0.2321	0.5655	0.3952	0.0479
$10^5$	0.5190	1.4884	0.1343	0.2352	0.5710	0.4064	0.0470

---

TABLE 2. Global quantities as defined in the text for hydrodynamic computations in the TM73 setup.

---

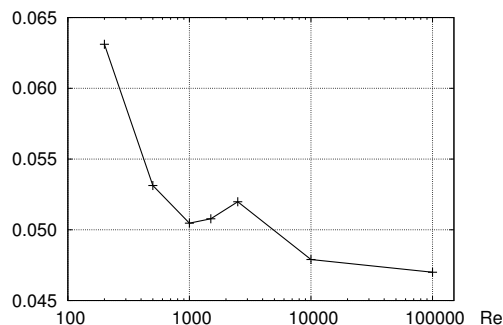


FIGURE 6. Time-averaged  $\overline{K_p}$  vs  $R_e$  in log-lin showing a crisis around  $R_e = 2.5 \times 10^3$ .

307 coherent with the theoretical arguments and the experimental observations from Cortet  
 308 et al. (2009).

309 In conclusion, even though our computations are performed at smaller  $R_e$  than in the  
 310 experiment, the trend followed by the global quantities compares well with the experi-  
 311 mental results of Ravelet et al. (2008).

### 3.3. Kinetic energy vs. Reynolds number

312 We investigate in this section the behavior of the kinetic energy as the kinetic Reynolds  
 313 number increases.

314 We show in figure 7(a) the time evolution of the kinetic energy  $E(t)$  for the Reynolds  
 315 numbers in the range  $\{2 \times 10^2, 5 \times 10^2, 10^3, 1.5 \times 10^3, 2.5 \times 10^3, 10^4, 10^5\}$ . There is a unique  
 316 time series since we have used the final state from the previous run as the initial condition  
 317 for the next run with a higher Reynolds number. We observe that the flow is steady at  
 318  $R_e = 2 \times 10^2$ . It is marginally unsteady at  $R_e = 5 \times 10^2$ , and increasing further  $R_e$  leads  
 319 to a turbulent regime. The time averaged kinetic energy  $\overline{E}$  increases with  $R_e$  as reported  
 320 in table 2.

321 Letting  $\hat{\mathbf{u}}(r, m, z, t)$  be the  $m$ -th complex Fourier component of the velocity field  
 322  $\mathbf{u}(r, \theta, z, t)$ , we define the kinetic energy of the  $m$ -th Fourier mode by

$$E_m = \int_{\Omega_{\text{fluid}}^{2D}} \pi |\hat{\mathbf{u}}(r, m, z, t)|^2 r dr dz. \quad (3.6)$$

324 Figure 7(b-c) shows  $E_m$  as a function of  $m$  for  $m \in \{0, \dots, 63\}$ . The maximum at  $m = 0$   
 325 corresponds to the large scale forcing induced by the rotating disk. The maximum at  
 326  $m = 8$  and the maxima at the corresponding harmonics are induced by the 8 rotating  
 327 blades. As expected, only the Fourier mode  $m = 0$  and the mode  $m = 8$  together with

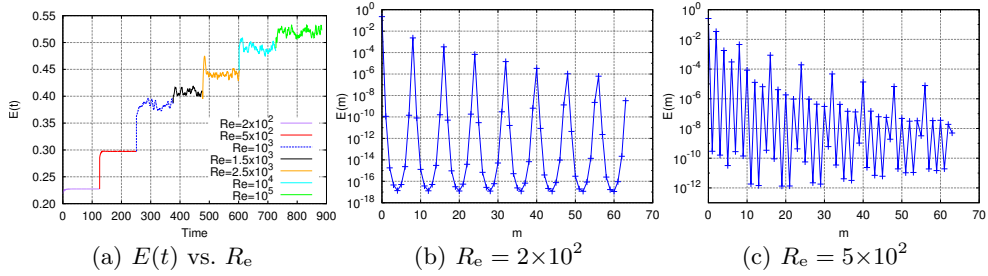


FIGURE 7. (a) Time evolution of the total kinetic energy  $E(t)$  vs.  $Re$ . Modal kinetic energy  $E_m$  as a function of the azimuthal Fourier mode: (b)  $Re = 2 \times 10^2$ ; (c)  $Re = 5 \times 10^2$ .

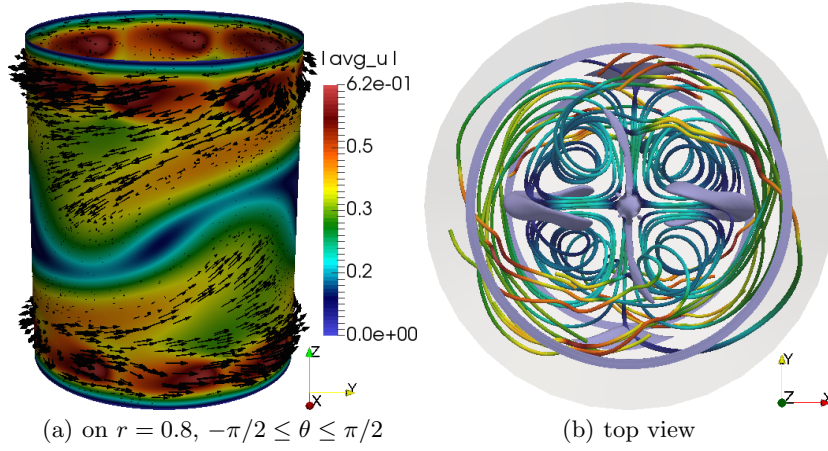


FIGURE 8. Navier-Stokes simulations in the TM73 VKS2 configuration at  $Re = 5 \times 10^2$ : (a) instantaneous velocity vector field on a cylindrical surface at  $r = 0.8$  for  $-\pi/2 \leq \theta \leq \pi/2$ ; (b) isosurface of 6% of the maximum velocity magnitude (purple) with streamlines (colored by velocity magnitude) from a top view; the cylinder  $\{r = 1\}$  is in light grey.

its harmonics are populated at  $Re = 2 \times 10^2$ . This scenario changes when the Reynolds number is slightly increased since all the even Fourier modes are active at  $Re = 5 \times 10^2$ .

At  $Re = 5 \times 10^2$  the flow is dominated by the Fourier modes  $m = 0$  and  $m = 2$  as illustrated in Figure 8. The left panel in the figure shows that the azimuthal shear layer near the equator acquires a wavy structure with two co-rotating radial vortices. This phenomenon has also been observed in Ravelet et al. (2008). The dominance of the Fourier mode  $m = 2$  and its harmonics is clearly seen when inspecting the velocity streamlines in figure 8(b). The spectrum in figure 7(c) shows that all the even modes are populated by nonlinearity.

As  $Re$  increases further, the axisymmetric mode  $m = 0$  and the Fourier mode  $m = 8$  together with its harmonics are still energetic, but the dynamics becomes richer as the mode  $m = 3$  starts to be active and eventually becomes the second largest after the axisymmetric mode (see figure 4). This  $m = 3$  structure has been visualized in the experiment at very high Reynolds numbers as reported in Cortet et al. (2009). The structure consists of three radial co-rotating vortices located nearby the equatorial shear layer. The Fourier modes  $m \in \{0, 3, 8\}$  eventually populate the entire spectrum by nonlinearity, and the spectrum has a more continuous appearance as  $Re$  grows (see figure 9). The quantity  $E_m$  decreases like a negative power of  $m$  when  $m$  is large. For instance  $E_m \sim m^{-5}$  for

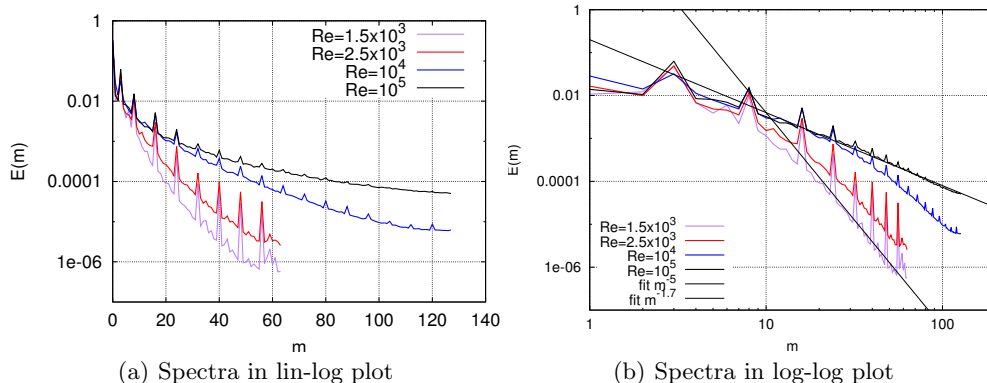


FIGURE 9. Spectra of the kinetic energy  $E_m$  as a function of the azimuthal mode at final time for  $R_e = 1.5 \times 10^3, 2.5 \times 10^3, 10^4, 10^5$ : (a) in lin-log scale, (b) in log-log scale with a fit in  $m^{-5}$  and in  $m^{-1.7}$  for guiding the eye.

346  $R_e = 1.5 \times 10^3$  and  $E_m \sim m^{-1.7}$  for  $R_e = 10^5$ . The scaling  $E_m \sim m^{-1.7}$  at  $R_e = 10^5$  is  
 347 close to  $m^{-5/3}$  and thereby reminiscent of the Kolmogorov 1941 turbulent scaling for a  
 348 one-dimensional kinetic energy spectrum (Frisch (1995)).

349 Let us finish this section by noting that a bifurcation similar to the one discussed  
 350 above, from even modes to odd modes, has been observed and reported in Herbert et al.  
 351 (2014) for TM60 impellers at  $R_e = 700$ . The TM60 configuration is slightly different from  
 352 the TM73 though; the blades in the TM60 setup are more curved and the impellers are  
 353 equipped with 16 blades instead of 8. The bifurcation was attributed to a ( $m = 1$ ) bifurca-  
 354 tion. However the use of planar S-PIV data made uneasy the discrimination between  
 355 odd modes like  $m = 1$  and  $m = 3$ . Also the shape and the number of the blades can  
 356 play a role in selecting the successive azimuthal dominating modes. In this reference the  
 357 authors have shown that increasing  $R_e$  from  $10^2$  to  $10^6$  leads to non-axisymmetric mod-  
 358 ulations of the axisymmetric (laminar or time-averaged) flow with successive azimuthal  
 359 changes in parity (even-odd-even-odd).

#### 360 4. MHD results

361 In this section we solve the full MHD system (2.1a)–(2.1d) using as initial velocity field  
 362 the velocity computed during the Navier-Stokes runs at the different  $R_e$ . The magnetic  
 363 field  $\mathbf{H} = \mathbf{B}/\mu_0\mu_r$  is initialized to a very small value which we call seed. Unless specified  
 364 otherwise, the seed is  $\mathbf{H}_0 = 10^{-3}(\mathbf{e}_z + \mathbf{e}_x)$ . We also add a random noise of amplitude  
 365  $5 \times 10^{-5}$  on all the Fourier modes  $m \geq 1$  of  $\mathbf{H}_0$ . We first explain how we determine the  
 366 threshold for dynamo action on an illustrative case. Next we study the influence of the  
 367 relative magnetic permeability of the impellers and the boundary conditions imposed on  
 368 the outer boundaries of the domain  $\Omega \cup \Omega_{\text{out}}$ . We then fix the relative magnetic perme-  
 369 ability of the impellers and use the pseudo-vacuum boundary conditions to investigate  
 370 the variation of the critical magnetic Reynolds number with  $R_e$ .

##### 371 4.1. Summary of our previous results

372 We have shown in Nore, C. et al. (2016) that two distinct dynamo families compete  
 373 at small Reynolds numbers (typically for  $R_e < 700$ ) and that these two families merge  
 374 at larger kinetic Reynolds numbers. In the first family, the magnetic field is essentially  
 375 supported on the even Fourier modes, whereas in the second family the magnetic field is

376 essentially supported on the odd modes; these are called the 0-family and the 1-family  
 377 in Nore, C. et al. (2016), respectively. In the entire section we focus on  $R_e \geq 1.5 \times 10^3$ ;  
 378 hence all the Fourier modes of the magnetic field are coupled and vary in time with the  
 379 same (growth or decay) rate in the linear dynamo regime.

380 4.2. *Dynamo threshold and saturation*

381 In this section we fix  $R_e = 10^4$  and explain how we estimate the dynamo threshold  
 382 with  $\mu_r^{\text{imp}} = 50$  and the pseudo-vacuum boundary condition. We are going to use  
 383 the same methodology for all the other cases. The onset of dynamo action is moni-  
 384 tored by recording the time evolution of the magnetic energy in the conducting domain,  
 385  $M(t) = \frac{1}{2} \int_{\Omega \cup \Omega_{\text{out}}} \mathbf{H}(\mathbf{r}, t) \cdot \mathbf{B}(\mathbf{r}, t) \, d\mathbf{r} = \frac{1}{2} \int_{\Omega \cup \Omega_{\text{out}}} \mu_0 \mu_r |\mathbf{H}(\mathbf{r}, t)|^2 \, d\mathbf{r}$ , and the modal energies  
 386  $M_m(t) = \int_{\Omega^{2D} \cup \Omega_{\text{out}}^{2D}} \pi |\hat{\mathbf{H}}(r, m, z, t)|^2 r \, dr \, dz$ . Linear dynamo action occurs when  $M_m(t)$  in-  
 387 creases exponentially in time (non oscillating dynamo here) and nonlinear dynamo action  
 388 takes place when  $M(t)$  saturates. Various MHD runs are performed with different values  
 389 of the magnetic Reynolds number  $R_m$ . The threshold for dynamo action is obtained by  
 390 interpolation on the growth rate between the largest magnetic Reynolds number with a  
 391 negative growth rate and the smallest magnetic Reynolds number with a positive growth  
 392 rate. The interpolation is done once the bracketing interval of the threshold is small  
 393 enough to yield a reasonable estimate.

394 4.2.1. *Linear regime*

395 The time evolution of the modal magnetic energies for the Fourier modes  $m \in \{0 \dots 4\}$   
 396 reported in figure 10 for  $R_m = 50$  and  $R_m = 150$  shows that the modes  $m = 0$  and  
 397  $m = 3$  of the magnetic field are coupled; this coupling is a consequence of the pre-  
 398 dominance of the mode  $m = 3$  in the velocity field (see figure 9). Due to the strong  
 399 hydrodynamical nonlinearities at this Reynolds number,  $R_e = 10^4$ , all the Fourier modes  
 400 of the magnetic field have the same decay or growth-rate. After estimating the de-  
 401 cay rate at  $R_m = 50$  and the growth rate at  $R_m = 150$ , linear interpolation shows  
 402 that the threshold in the considered conditions is  $R_m^c = 75 \pm 5$ . All the thresholds on  
 403  $R_m$  for dynamo action with  $\mu_r^{\text{imp}} = 50$ , the pseudo-vacuum boundary condition, and  
 404  $R_e \in \{2 \times 10^2, 5 \times 10^2, 10^3, 1.5 \times 10^3, 2.5 \times 10^2, 10^4, 10^5\}$  are reported in table 4.

405 We show in figure 11 the distribution of the modal energies  $E_m$  and  $M_m$  at two different  
 406 times for  $R_m = 150$ . Note that there is dynamo action at this magnetic Reynolds number.  
 407 The graphs in the left panel (figure 11(a)) have been done during the linear growth of the  
 408 magnetic field. Those in the right panel (figure 11(b)) have been obtained at saturation.  
 409 Note that the spectrum of the magnetic energy during the linear growth resembles that of  
 410 the kinetic energy; the Fourier modes  $m \in \{0, 3\}$  and the mode  $m = 8$  with its harmonics  
 411 are dominant.

412 4.2.2. *Nonlinear regime*

413 At  $R_m = 150$  we have  $R_m \approx 2 \times 75 = 2R_m^c$ ; hence the simulation done at  $R_m = 150$  is  
 414 far from the threshold, and the Lorentz force is therefore strong enough to retroact on the  
 415 velocity field in the saturated phase. Figure 11(b) shows that the small azimuthal modes  
 416 ( $m \in \{0 \dots 4\}$ ) of the velocity field and the magnetic field are indeed in competition  
 417 at saturation ( $t = 1300$ ); this can be seen also in figure 10(b) in the time interval  $t \in$   
 418  $[1210, 1300]$ . The dominant Fourier modes of the velocity in the saturated regime are now  
 419  $m \in \{0, 1, 2\}$  as seen in figure 12(a). The kinetic energy decreases while the magnetic  
 420 energy increases during the time interval  $t \in [1100, 1240]$  as shown in figure 12(b); at  
 421  $t = 1250$  both quantities have reached asymptotic values about which they fluctuate.  
 422 The retroaction of the Lorentz force makes the torque decrease by 40%; hence driving



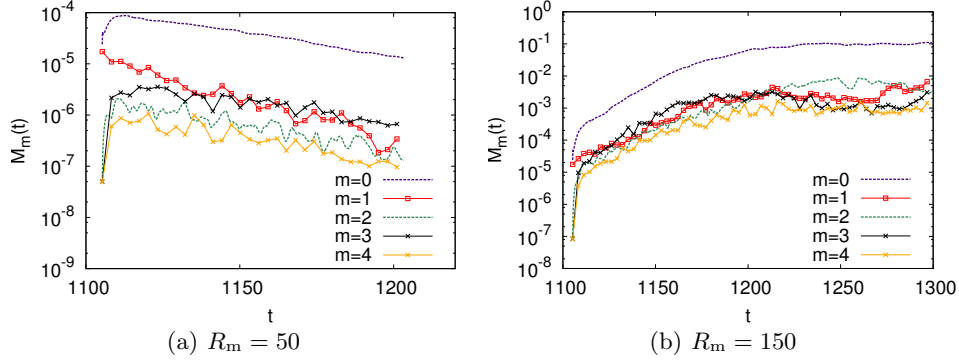


FIGURE 10. Time evolution of the modal magnetic energies  $M_m(t)$  at  $R_e = 10^4$  with  $\mu_r^{\text{imp}} = 50$  for  $m \in \{0 \dots 4\}$ : (a)  $R_m = 50$ ; (b)  $R_m = 150$ .

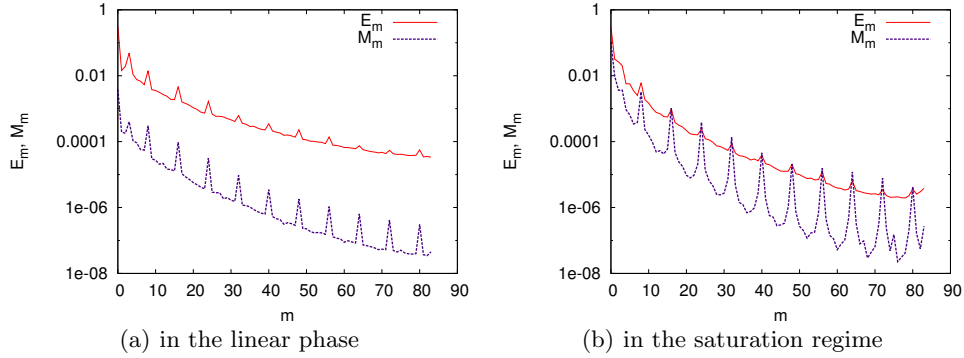


FIGURE 11. Spectra of the kinetic  $E_m$  and magnetic  $M_m$  energies as a function of the azimuthal mode for  $R_e = 10^4$  and  $R_m = 150$ : (a) in the linear phase at  $t = 1142$ ; (b) in the saturation regime at  $t = 1300$ .

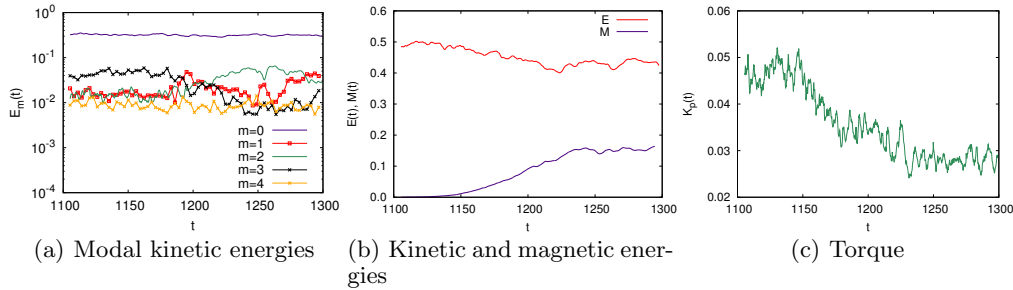


FIGURE 12. Time evolution of (a) the modal kinetic energies  $E_m(t)$  for  $m \in \{0 \dots 4\}$  and for  $R_m = 150$ ,  $R_e = 10^4$  and  $\mu_r^{\text{imp}} = 50$ , (b) the kinetic and magnetic energies and (c) the total torque.

423 the dynamo saturated flow requires less mechanical power than driving the hydrodynamic  
 424 base flow (see figure 12(c)).

425 While the retroaction of the Lorentz force on the velocity field in turbulent flows has  
 426 been studied in various experiments involving applied magnetic fields (see e.g. Sisan  
 427 et al. (2003); Miralles et al. (2015)), very little is known in this respect when dynamo

428 action occurs. In the Riga experiment, an increase of about 10% of the power consump-  
 429 tion has been measured at saturation, and a modification of the swirling profile together  
 430 with a deceleration of the axial motion has been observed (Gailitis et al. (2003)). In  
 431 the Karlsruhe experiment, a slow down of the axial flow has been recorded in the non-  
 432 linear regime (Müller et al. (2004)). In the VKS2 experiment, the modification of the  
 433 flow in the saturation regime has been too weak to be measured. Note that the range  
 434 of magnetic Reynolds numbers that can be explored experimentally is limited by the  
 435 mechanical power that is available; in the above three experiments dynamo action has  
 436 been investigated only in a small neighborhood beyond the threshold.

437 Although very interesting, the study of the nonlinear regime over a large range of  
 438 parameters is numerically expensive and therefore postponed for future work.

#### 439 4.3. Impact of the magnetic permeability and boundary conditions on the threshold

440 We focus in this section on the influence of various parameters on the threshold and we  
 441 investigate the structure of the growing magnetic field.

##### 442 4.3.1. Influence of the magnetic permeability

443 In this section we work with the pseudo-vacuum boundary condition enforced at the  
 444 outer boundary of the domain  $\Omega \cup \Omega_{\text{out}}$ ; this boundary condition corresponds to setting  
 445  $\mathbf{H} \times \mathbf{n} = \mathbf{0}$ , and it is also called perfect ferromagnetic boundary condition in the litera-  
 446 ture. We also fix the Reynolds number to  $R_e = 1.5 \times 10^3$ . Figures 13(a-e) show the time  
 447 evolution of  $M_m(t)$  for the azimuthal modes  $m \in \{0 \dots 4\}$  for  $\mu_r^{\text{imp}} = 1$  and  $\mu_r^{\text{imp}} = 5$ .  
 448 When  $\mu_r^{\text{imp}} = 1$  and near criticality, the behavior of the magnetic field shows a competi-  
 449 tion between the modes  $m = 0$  and  $m = 1$  ( $R_m = 100, 200$  in figures 13(a-b)). Well  
 450 above the threshold, say at  $R_m = 300$  and beyond, we recover the same dynamics as that  
 451 obtained when  $\mu_r^{\text{imp}}$  is larger; that is, the axisymmetric magnetic field is dominant and it  
 452 is preferentially coupled to the mode  $m = 3$  through the velocity field. The threshold for  
 453  $\mu_r^{\text{imp}} = 1$  is estimated to be  $R_m^c = 190 \pm 10$ . The threshold for  $\mu_r^{\text{imp}} = 5$  is estimated to be  
 454  $R_m^c = 170 \pm 5$ . This value is slightly higher than the value  $R_m^c \approx 130$  reported in Nore, C.  
 455 et al. (2016). The likely origin of the discrepancy is that for the present simulations the  
 456 initial seed for the magnetic field is  $\mathbf{H}_0 = 10^{-6}(\mathbf{e}_z + \mathbf{e}_x)$  plus a random noise of amplitude  
 457  $5 \times 10^{-7}$  on all the Fourier modes  $m \geq 1$  of  $\mathbf{H}_0$  and the integration time is longer. Hence  
 458 the present estimation is probably more accurate. It seems that for small values of  $\mu_r^{\text{imp}}$ ,  
 459 typically  $\mu_r^{\text{imp}} \leq 5$ , the dynamics is more complicated and involves interactions between  
 460 modes that depend on the level of the nonlinearities implicated. The key observation  
 461 here is that the axisymmetric mode is reinforced when  $\mu_r$  is large. This in turn gives a  
 462 clearer decay or growth rate and consequently makes it easier to estimate the threshold.  
 463 The largest value of the relative permeability used in the present paper is  $\mu_r^{\text{imp}} = 50$ .

##### 464 4.3.2. Influence of the boundary conditions

465 To test the influence of boundary conditions, we now enlarge the computational domain  
 466 by adding an insulator around the VKS2 container (air or vacuum). The outer boundary  
 467 of the computational domain is now a sphere centered at the origin and of radius 10. The  
 468 magnetic field in the insulator is represented as the gradient of a scalar potential like  
 469 in Guermond et al. (2009) and this potential is enforced to be zero on the outer sphere.  
 470 This configuration is a better representation of the actual experiment than that with the  
 471 pseudo-vacuum boundary condition, but it is computationally more expensive.

472 We show in figure 14 the time evolution of the magnetic energy at  $R_e = 1.5 \times 10^3$  for the  
 473 Fourier modes  $m \in \{0 \dots 4\}$  with  $\mu_r^{\text{imp}} = 1$  (panels (a-b)) and with  $\mu_r^{\text{imp}} = 50$  (panels (c-  
 474 d)). These computations have been done with the vacuum boundary condition. The seed

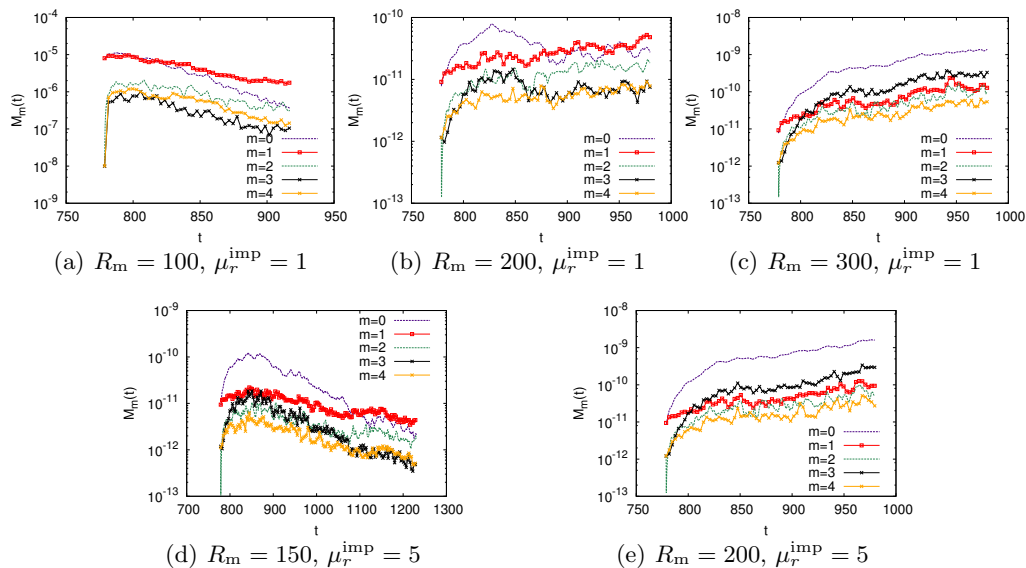


FIGURE 13. Time evolution of  $M_m(t)$  at  $R_e = 1.5 \times 10^3$  with pseudo-vacuum BC for  $m \in \{0 \dots 4\}$ : (a-c)  $R_m \in \{100, 200, 300\}$  and  $\mu_r^{\text{imp}} = 1$ ; (d-e)  $R_m \in \{150, 200\}$  and  $\mu_r^{\text{imp}} = 5$ .

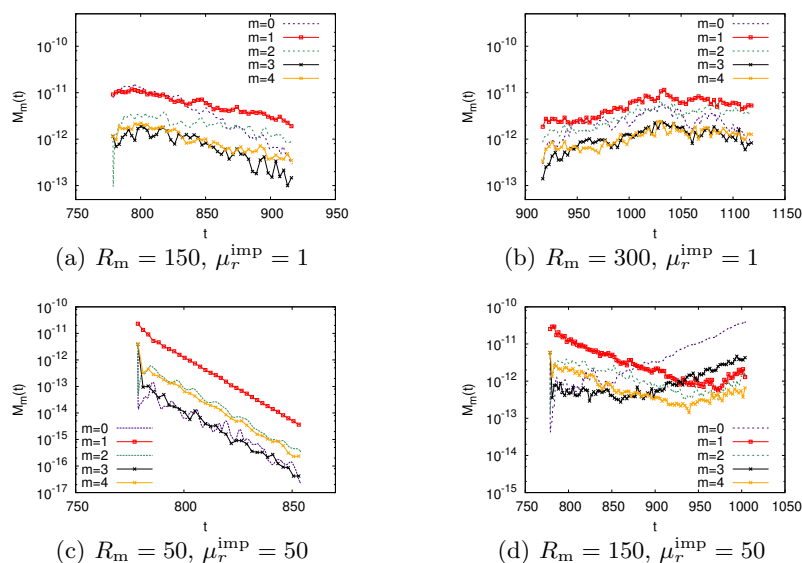


FIGURE 14. Time evolution of  $M_m(t)$  at  $R_e = 1.5 \times 10^3$  with vacuum BC for  $m \in \{0 \dots 4\}$ : (a-b)  $R_m \in \{150, 300\}$  and  $\mu_r^{\text{imp}} = 1$ ; (c-d)  $R_m \in \{50, 150\}$  and  $\mu_r^{\text{imp}} = 50$ .

475 for the magnetic field is  $\mathbf{H}_0 = 10^{-6} \mathbf{e}_x$  plus a random noise of amplitude  $5 \times 10^{-7}$ . We  
 476 removed the axial component of the seed to convince ourselves unequivocally that the  
 477 axial component of the axisymmetric mode grows above the dynamo threshold.

478 For  $\mu_r^{\text{imp}} = 1$ , the two Fourier modes  $m = 1$  and  $m = 2$  compete below and above the  
 479 threshold. The threshold in this case is larger than when the pseudo-vacuum boundary  
 480 condition is imposed. We obtain here  $R_m^c = 310 \pm 30$  whereas we had  $R_m^c = 190 \pm 10$   
 481 with the pseudo-vacuum boundary condition. The increase is roughly 60%. The magnetic

B.C.	$\mu_r^{\text{imp}}$	$R_m^c$	Dominant mode	Figure
$\mathbf{H} \times \mathbf{n} = \mathbf{0}$	1	$190 \pm 10$	0, 1	fig. 13(a-c)
$\mathbf{H} \times \mathbf{n} = \mathbf{0}$	5	$170 \pm 5$	0, 1	fig. 13(d-e)
$\mathbf{H} \times \mathbf{n} = \mathbf{0}$	50	$90 \pm 5$	0	fig. 6 in Nore, C. et al. (2016)
vacuum	1	$310 \pm 30$	1	figs 14(a-b) & 15(a-b)
vacuum	50	$130 \pm 10$	0	figs 14(c-d) & 15(c-d)

TABLE 3. Magnetic thresholds  $R_m^c$  for  $R_e = 1.5 \times 10^3$ . “ $\mathbf{H} \times \mathbf{n} = \mathbf{0}$ ” means pseudo-vacuum boundary condition and “vacuum” means that a larger integration domain with a non-conducting domain around the outer cylinder is used.

482 field is mainly supported on the Fourier modes  $m = 1$  and  $m = 2$  with a complex three-  
 483 dimensional structure as shown on figure 15(a-c).

484 For  $\mu_r^{\text{imp}} = 50$  the threshold is estimated to be at  $R_m^c = 130 \pm 10$  (figure 14(c-d)).  
 485 Inspection of figure 14(d) reveals that at  $R_m = 150$  the Fourier mode  $m = 1$  decreases  
 486 in time, while the modes  $m = 0$  and  $m = 3$  increase and pull in their wake the other  
 487 modes for  $t \geq 850$ . This scenario is reminiscent of the crossing of the modes  $m = 1$  and  
 488  $m = 0$  discussed in Boisson and Dubrulle (2011). The present simulations show that  
 489 the magnetic field is not purely axisymmetric since a significant portion of the magnetic  
 490 energy is carried by the Fourier mode  $m = 3$ . We will examine the relative importance  
 491 of the non-axisymmetric modes in section 4.5. As shown in figure 15(d-f) the growing  
 492 magnetic field is mainly an axial dipole with an azimuthal component approximately  
 493 even in  $z$ . The structure of the instantaneous and average magnetic field (fig. 15(d-e)) is  
 494 similar to the one obtained with the pseudo-vacuum boundary condition (see fig. 17(a-  
 495 b)). This structure is also compatible with the measurements of the magnetic field made  
 496 at saturation during the dynamo regime obtained in the VKS2 configuration with soft  
 497 iron impellers and a copper container (see figure 6b in Boisson et al. (2012)).

498 When one compares the estimations of the threshold using  $\mu_r^{\text{imp}} = 50$  and the pseudo-  
 499 vacuum boundary condition,  $R_m^c = 90 \pm 5$ , with that obtained with  $\mu_r^{\text{imp}} = 50$  and the  
 500 vacuum boundary condition,  $R_m^c = 130 \pm 10$ , we observe a 40% increase. This dependence  
 501 of the dynamo threshold on the boundary condition is compatible with the observation  
 502 made in Guermond et al. (2011a); Gissinger et al. (2008) using kinematic dynamo simu-  
 503 lations. It is shown in these references that the perfect ferromagnetic boundary condition  
 504 decreases the dynamo threshold, the minimum being achieved when this boundary condi-  
 505 tion is enforced over the entire boundary of the container. This is explained by a screening  
 506 mechanism of the walls. The present full MHD simulations show the same trend.

507 The data collected in table 3 lead to the conclusion that using the ferromagnetic bound-  
 508 ary condition on the external boundary of the container and using ferromagnetic material  
 509 for the impeller with a large value of the magnetic permeability decreases the dynamo  
 510 threshold and enhances the axisymmetric component of the magnetic field produced by  
 511 the dynamo effect.

512 4.4. Threshold at  $\mu_r^{\text{imp}} = 50$  vs.  $R_e$

513 We put ourselves in this section in the most favorable configuration for dynamo action  
 514 to occur: we enforce the ferromagnetic boundary condition on the external boundary of  
 515 the container and we use  $\mu_r^{\text{imp}} = 50$ . We now investigate the evolution of the critical  
 516 magnetic Reynolds number as a function of the kinetic Reynolds number.

517 We have reported in Figure 16(a) the estimated value of  $R_m^c$  for  $R_e \in \{5 \times 10^2, 1.5 \times 10^3,$   
 518  $2.5 \times 10^3, 10^4, 10^5\}$ . The critical magnetic Reynolds number seems to tend to an asymp-

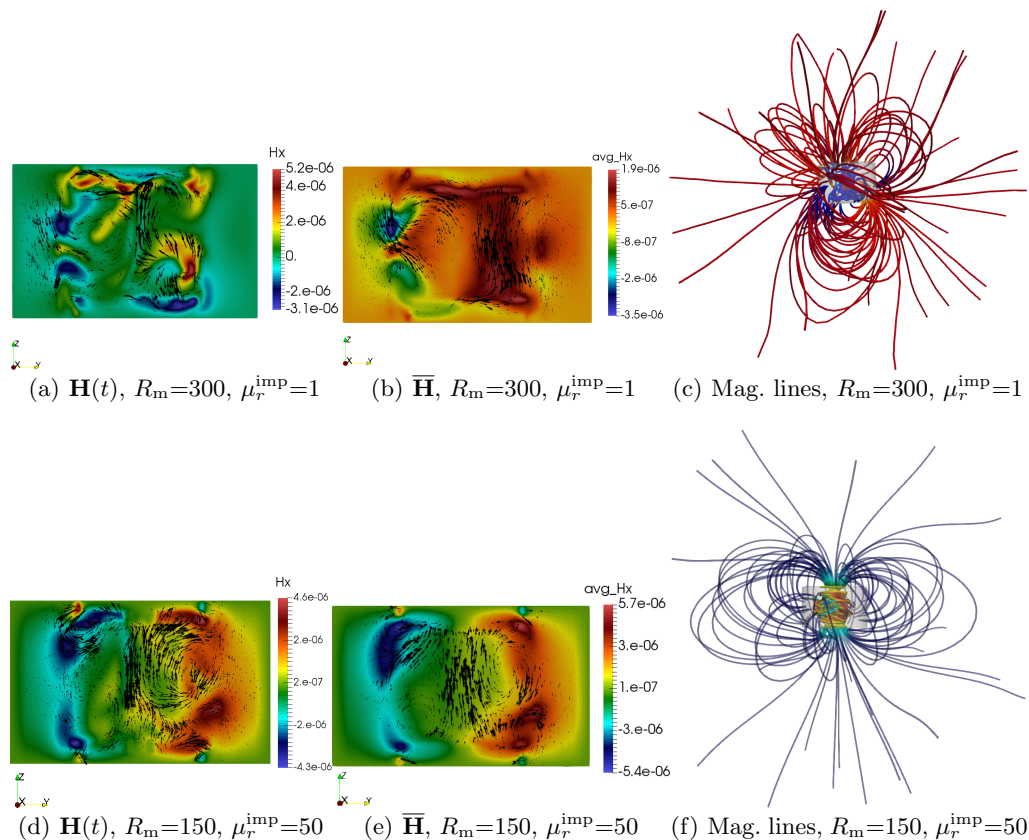


FIGURE 15. Magnetic field from full MHD simulations in the TM73 VKS2 configuration at  $Re = 1.5 \times 10^3$  with vacuum BC: (a-b)  $R_m = 300$ ,  $\mu_r^{\text{imp}} = 1$ , instantaneous and time averaged magnetic field in  $\Omega_c$ ; (c)  $R_m = 300$ ,  $\mu_r^{\text{imp}} = 1$ , magnetic field lines in the whole domain; (d-e)  $R_m = 150$ ,  $\mu_r^{\text{imp}} = 50$ , instantaneous and time averaged magnetic field in  $\Omega_c$ ; (f)  $R_m = 150$ ,  $\mu_r^{\text{imp}} = 50$ , magnetic field lines in the whole domain. In (a,b,d,e) arrows represent in-plane  $\{H_y, H_z\}$  vectors and color represents the out-of-plane component  $H_x$ .

---

$R_e$	$5 \times 10^2$	$1.5 \times 10^3$	$2.5 \times 10^3$	$10^4$	$10^5$
$R_m^c$	$135^* \pm 5$	$90^* \pm 5$	$85 \pm 5$	$75 \pm 5$	$70 \pm 5$
$P_m^c$	$\approx 0.27^*$	$\approx 0.06^*$	$\approx 0.034$	$7.5 \times 10^{-3}$	$7 \times 10^{-4}$

TABLE 4. Magnetic thresholds  $R_m^c$  and critical magnetic Prandtl numbers  $P_m^c$  for  $\mu_r^{\text{imp}} = 50$  versus fluid Reynolds number  $R_e$ . Asterisk designates values from Nore, C. et al. (2016).

---

519 totic value  $R_{m\infty}^c$  as the kinetic Reynolds number tends to infinity. To better quantify  
 520 this observation we represent in figure 16(b) in log-log scale the difference  $R_m^c - R_{m\infty}^c$  as  
 521 a function of  $R_e$ , with  $R_{m\infty}^c = 68.8$ , and we compare our numerical estimations with the  
 522 ansatz  $R_m^c - R_{m\infty}^c = 4100/R_e^{0.7}$ . The match is excellent. But we must stay realistic since  
 523 we have fitted five points with three somewhat ad hoc constants: 0.7, 68.8, and 4100. Nev-  
 524 ertheless, recalling the definition  $R_m := \mu_0 \sigma 2\pi f R_{\text{cyl}}^2$ , it is remarkable that  $R_{m\infty}^c = 68.8$   
 525 is in the range [52, 71] where dynamo action has been observed in the VKS2 experiment,  
 526 as explained in section 2.1.

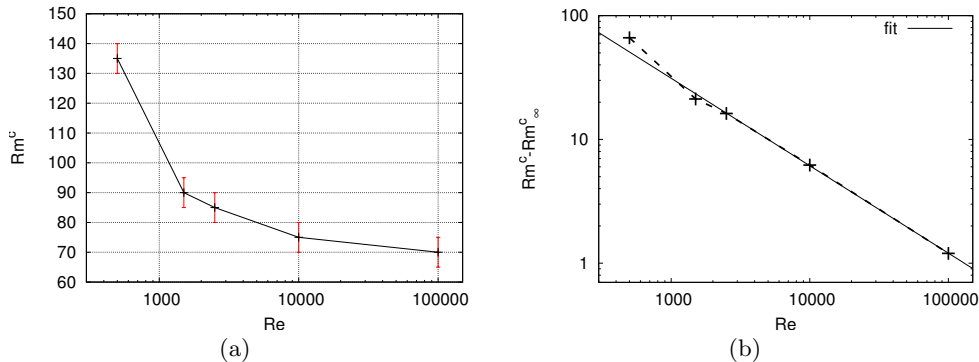


FIGURE 16. (a)  $R_m^c$  vs.  $R_e$  in log-lin; (b)  $R_m^c - R_{m\infty}^c$  vs.  $R_e$  in log-log using the fit  $4100/R_e^{0.7}$ .

527 Assuming, as suggested by the results reported in table 3, that going from  $\mu_r^{\text{imp}} \approx 50$   
 528 to  $\mu_r^{\text{imp}} = 1$  doubles the threshold for dynamo action (uniformly in  $R_e$ ), we conjecture  
 529 that the asymptotic limit  $R_{m\infty}^c$  for  $\mu_r^{\text{imp}} = 1$  is roughly  $68.8 \times 2 \approx 138$ . The estimate  
 530 of the threshold obtained experimentally by measurements of the decay time in this  
 531 configuration (run O in figure 6 of Miralles et al. (2013), Table I, and definition of  $R_m$   
 532 at line -12, page 8) gives  $R_m^c \simeq 110$ , which is in good agreement with our conjecture  
 533 considering that the ferromagnetic walls in run O are closer to the impellers than in our  
 534 computations.

#### 535 4.5. Shape of the magnetic field vs $R_e$

536 We continue with the pseudo-vacuum boundary conditions and  $\mu_r^{\text{imp}} = 50$ . Figures 17  
 537 and 18 show the instantaneous and the time averaged magnetic fields obtained at satu-  
 538 ration in the dynamo regime at  $R_e = 1.5 \times 10^3$  and  $R_e = 10^5$ , respectively. Note that  
 539 the instantaneous magnetic field at  $R_e = 10^5$  shows bursts near the impellers, although  
 540 the time averaged magnetic field for  $R_e = 1.5 \times 10^3$  and  $R_e = 10^5$  are similar. Note also  
 541 that the time averaged magnetic vector field in the  $yOz$  plane is not strictly symmetric  
 542 with respect to the  $Oz$  axis. The ratio of the non-axisymmetric magnetic energy to the  
 543 total magnetic energy is about 11% for  $R_e = 1.5 \times 10^3$ ,  $R_m = 150$ , and it is about 18%  
 544 for  $R_e = 10^5$ ,  $R_m = 100$ . This little departure from axisymmetry gives a wavy shape to  
 545 the magnetic field streamlines as shown in figure 17(c) and figure 18(c). The dominant  
 546 non-axisymmetric Fourier mode of the magnetic field is  $m = 3$  as shown in figures 17(d-e)  
 547 and 18(d-e).

548 Although the flows at  $R_e = 1.5 \times 10^3$  and  $R_e = 10^5$  are quite different, the time aver-  
 549 aged magnetic fields produced by dynamo action are very similar: compare figure 17(b)  
 550 and figure 18(b). This observation leads us to conjecture that the time averaged mag-  
 551 netic field should have the same shape for the actual Reynolds number  $R_e \approx 5 \times 10^6$ .  
 552 At least the axisymmetric shape in figure 17(b) and figure 18(b) is similar to the one  
 553 reconstructed in fig. 6(b) in Boisson et al. (2012). Of course, the scarcity of experimen-  
 554 tal data (gaussmeters on a few lines) gives little information on the non-axisymmetric  
 555 components.

## 556 5. Simplified models

557 Upon observing that the spectrum of the growing magnetic field is dominated by the  
 558 azimuthal Fourier modes  $m = 0$  and  $m = 3$  (see figure 11(a)), one may wonder if the  
 559 dynamo effect is associated with the 3 co-rotating vortices localized in the equatorial

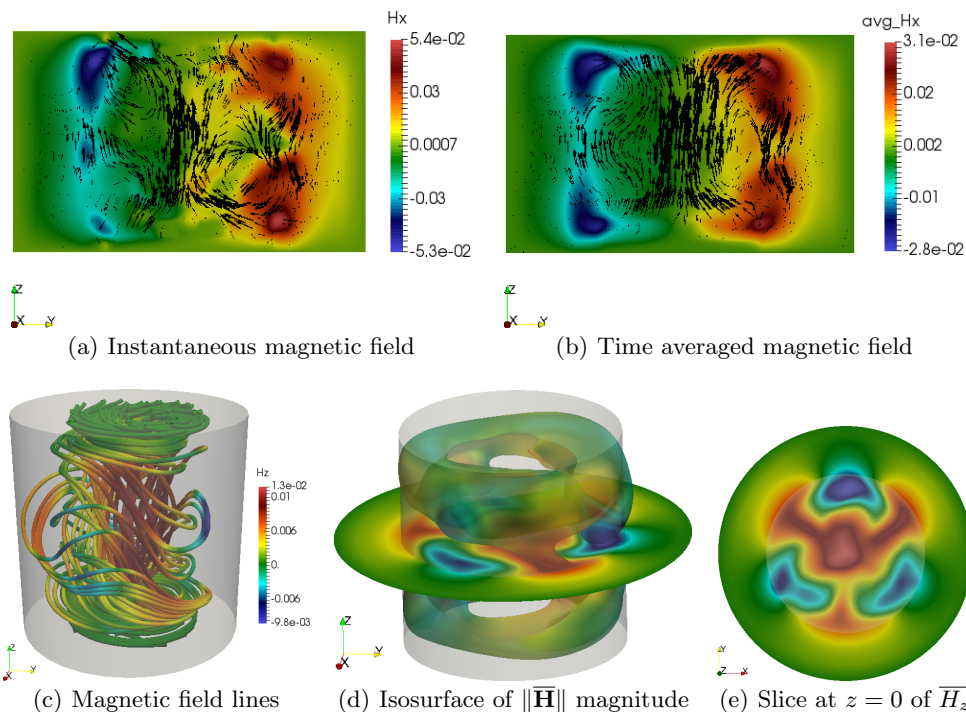


FIGURE 17. Magnetic field from full MHD simulations in the TM73 VKS2 configuration in the saturated regime at  $R_e = 1.5 \times 10^3$ ,  $R_m = 150$  and  $\mu_r^{\text{imp}} = 50$ , pseudo-vacuum BC: (a)-(b) Arrows represent in-plane  $\{H_y, H_z\}$  vectors, color represents the out-of-plane component  $H_x$ , the cylinder axis is in the middle. (From Nore, C. et al. (2016)); (c) Magnetic field lines of  $\overline{\mathbf{H}}$  colored by  $\overline{H_z}$ ; (d) Isosurface of 50% of the maximum amplitude of  $\|\overline{\mathbf{H}}\|$  and cut at  $z = 0$  for  $\{r \leq 1.6\}$ ; (e) Cut at  $z = 0$  from top view colored by  $\overline{H_z}$  (the inner cylinder of radius  $r = 1$  is indicated in light grey, the outer radius is 1.6).

560 shear layer or if the ferromagnetic impeller is the key ingredient as discussed in Pétrélis  
 561 et al. (2007); Laguerre et al. (2008); Gissinger et al. (2008). To try to answer this question,  
 562 we first perform kinematic dynamo computations using the time average of the velocity  
 563 field obtained at  $R_e = 10^5$  and shown in figure 4. Then, we take a closer look at the  
 564 structure of the electrical current that is generated by dynamo action in the full MHD  
 565 simulations.

### 5.1. Kinematic dynamo using the time averaged velocity field at $R_e = 10^5$

567 A kinematic dynamo simulation is done by solving only the induction equation (2.1b)  
 568 and by using the time averaged velocity field obtained at  $R_e = 10^5$ ; this field is shown in  
 569 figure 4. The time averaged velocity field is not axisymmetric and therefore may sustain  
 570 an axisymmetric magnetic field since Cowling's theorem does not apply. We also use flat  
 571 ferromagnetic disks with  $\mu_r^{\text{imp}} = 50$  and we impose the boundary condition  $\mathbf{H} \times \mathbf{n} = \mathbf{0}$   
 572 on the outer wall of the container.

573 We perform simulations with  $R_m \in [50, 200]$  and find that the Fourier modes  $m \in$   
 574  $\{1, 2, 4\}$  can grow while the modes  $m \in \{0, 3\}$  always decrease. The dynamo threshold is  
 575  $R_m^c \approx 120 \pm 5$  and the growing magnetic field has a strong Fourier component supported  
 576 on the mode  $m = 1$ . This unstable eigenmode has the shape of an equatorial dipole  
 577 with two opposite axial structures (see figure 19). This magnetic field is similar to the

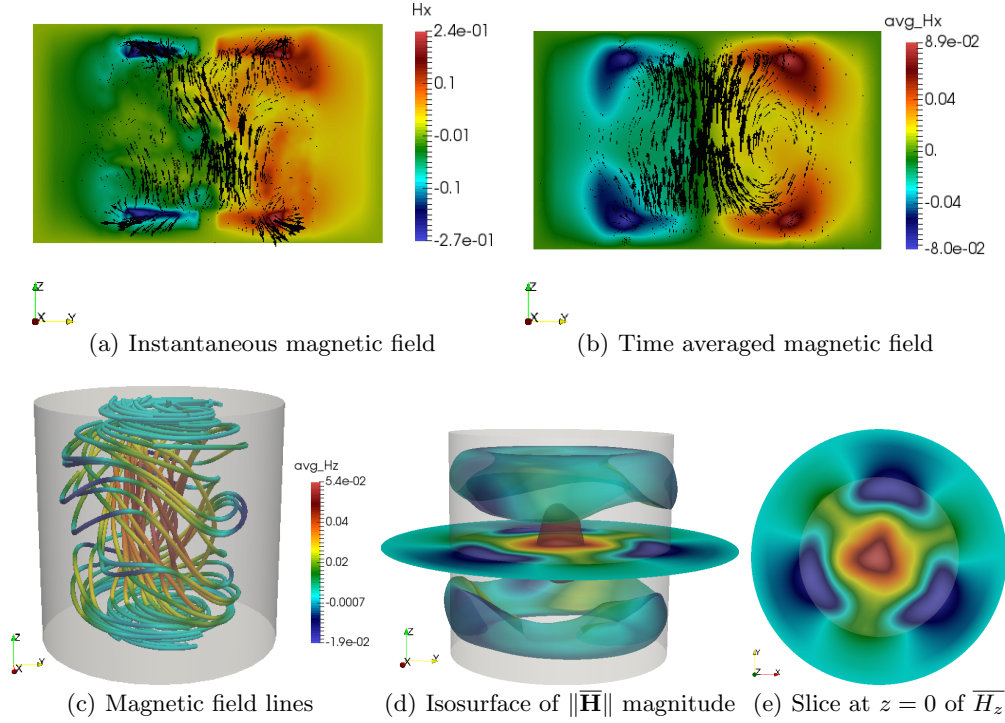


FIGURE 18. Same as figure 17 with  $R_e = 10^5$ ,  $R_m = 100$  and  $\mu_r^{\text{imp}} = 50$ .

one obtained using the time and azimuth averaged flow measured in a von Kármán experiment done in water (see e.g. Ravelet et al. (2005); Guermond et al. (2011a)). Once we take into account a velocity factor that has been applied to the dimensionless maximum value of the velocity (between 0.6 and 0.75), the threshold  $R_m^c \approx 120$  is in the range of those published in the above references; for instance  $43/0.75 \leq R_m^c \leq 180/0.6$  in Ravelet et al. (2005) and  $40/0.75 \leq R_m^c \leq 82/0.6$  in Guermond et al. (2011a).

The main point of the present discussion is that the kinematic dynamo realized with the time-averaged velocity field obtained at  $R_e = 10^5$  gives a dynamo that is totally different from the one obtained with the full velocity field since it is mainly supported on the Fourier mode  $m = 1$ . Therefore the mainly axisymmetric magnetic field shown in figure 18 cannot be attributed to the time averaged velocity field only.

### 5.2. Shape of the electric current vs. $R_e$

We now focus our attention on the electric current produced by the full MHD dynamo. Figures 20(a-b) show the electric current associated to the time averaged magnetic field computed at  $R_e = 1.5 \times 10^3$  with  $R_m = 150$ ; figures 20(c-d) show the electric current associated to the time averaged magnetic field computed at  $R_e = 10^5$  with  $R_m = 100$ . In both cases we use  $\mu_r^{\text{imp}} = 50$ . The current distribution shows large scale meridian loops. The current lines close to the axis have the shape of a left-handed helix going downwards; the current is mainly radial in the disks (flowing outwards in the bottom disk and inwards in the top disk); it is mainly vertical and flows upwards in the copper wall ( $j_z$  is positive in fig. 20(b-d) in the ring  $\{1.4 \leq r \leq 1.6; z = 0\}$ ). It also forms smaller meridian loops near the blades. The poloidal component of the current ( $\{j_r, j_z\}$  in the copper wall and near the blades) generates the toroidal  $H_\theta$  field, while the toroidal  $j_\theta$  component of the twisted helical current lines near the axis creates the axial  $H_z$  magnetic field. This organization



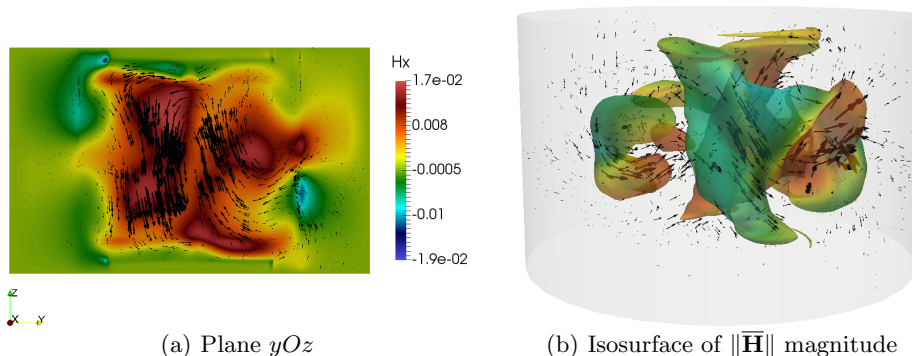


FIGURE 19. Magnetic field from kinematic dynamo simulations using the time averaged velocity field at  $Re = 10^5$  with  $R_m = 150$  and  $\mu_r^{\text{imp}} = 50$ : (a) arrows represent in-plane  $\{H_y, H_z\}$  vectors, color represents the out-of-plane component  $H_x$ , the cylinder axis is in the middle; (b) isosurface of the magnetic magnitude (colored by the  $H_z$  component: red for upward direction and green for downward direction) at 30% of the maximum with magnetic vector fields.

602 of the current evokes the disk-dynamo of Bullard (1955) with two disks (instead of one  
 603 only). The radial current in the bottom disk is collected in the copper walls, injected in  
 604 the top disk, and flows from the top disk to the bottom disk in a left-handed helix. The  
 605 left-hand twist of the current lines in the bulk near the cylinder axis is induced by the  
 606 flow of liquid sodium. Figure 21(a) shows the current lines colored by  $\|\mathbf{j}\|$ . The current  
 607 amplitude is strong near the axis. A schematic representation of the double-disk Bullard  
 608 dynamo is shown in Figure 21(b).

## 609 6. Summary and discussion

610 The main outcomes of the present paper are the following points:

611 (a) The hydrodynamic computations using the entropy-viscosity-based LES technique  
 612 give results in agreement with the experimental data at high Reynolds numbers. The  
 613 global experimental and numerical kinetic quantities behave similarly when  $Re$  increases.  
 614 The modal spectrum of the kinetic energy is dominated by the azimuthal Fourier modes  
 615  $m \in \{0, 2\}$  for  $Re < 700$  and  $m \in \{0, 3\}$  for larger  $Re$ . At  $Re = 10^5$ , the modal spectrum  
 616 behaves like  $m^{-5/3}$  when  $m$  is large. In the physical space, the leading Fourier mode  
 617  $m = 2$  found at  $Re = 5 \times 10^2$  corresponds to the wavy bifurcation reported in Ravelet  
 618 et al. (2008). At larger  $Re$ , the Fourier mode  $m = 3$  is related to the three radial co-  
 619 rotating vortices localized near the equatorial shear layer as observed by Cortet et al.  
 620 (2009) in a von Kármán experiment using water.

621 (b) The full MHD computations show that, at fixed  $Re$ , increasing the relative mag-  
 622 netic permeability of the impellers and/or using ferromagnetic material at the outer  
 623 boundaries of  $\Omega \cup \Omega_{\text{out}}$  decreases the threshold (using the pseudo-vacuum B.C. is equiva-  
 624 lent to adding a material with infinite permeability at the boundary). The ferromagnetic  
 625 impellers enhance the axisymmetric magnetic field (Giesecke et al. (2012)) and ferro-  
 626 magnetic outer walls confine the magnetic field inside the vessel. At fixed  $\mu_r$ , increasing  
 627 the kinetic Reynolds number also reduces the threshold. Moreover, the overall shape of  
 628 the critical magnetic field averaged in time barely changes between  $Re = 1.5 \times 10^3$  and  
 629  $Re = 10^5$  as shown in figures 17 and 18. This robustness with respect to the kinetic  
 630 Reynolds number may explain why the magnetic field that we computed is in very good  
 631 agreement with the mainly axisymmetric magnetic field that has been experimentally ob-

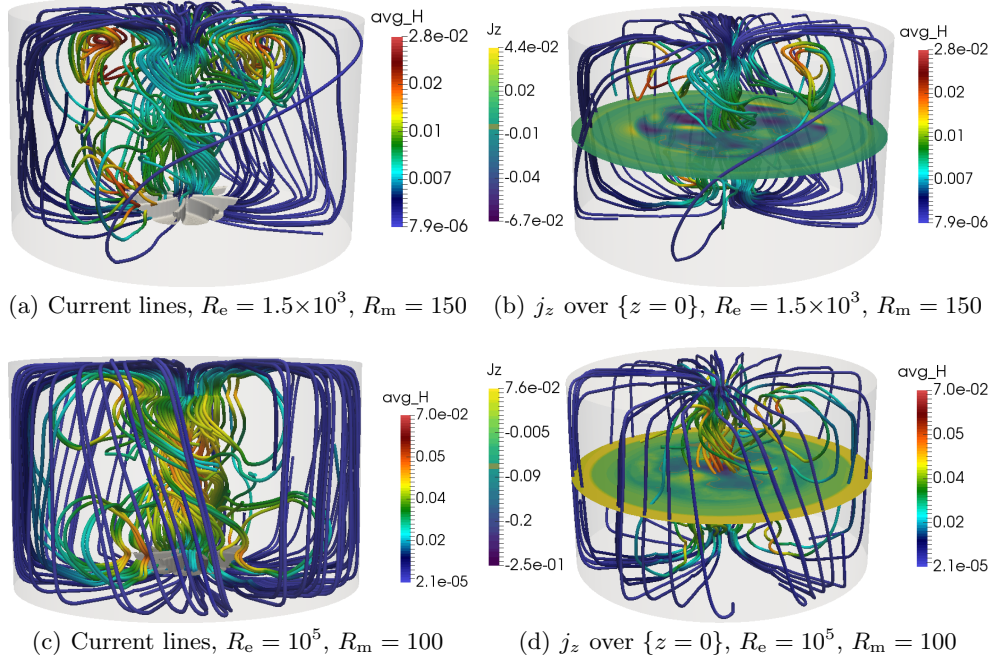


FIGURE 20. Electric current field from time averaged magnetic field,  $\mu_r^{\text{imp}} = 50$ : (a-b)  $R_e = 1.5 \times 10^3$ ,  $R_m = 150$ ; (c-d)  $R_e = 10^5$ ,  $R_m = 100$ ; (a-c) Streamlines of the current  $\vec{j} = \nabla \times \vec{H}$  colored by the magnitude of  $\|\vec{H}\|$ ; (b-d) Current streamlines colored by the magnitude of  $\|\vec{H}\|$  and slice at  $\{z = 0\}$  colored by  $\vec{j}_z$ .

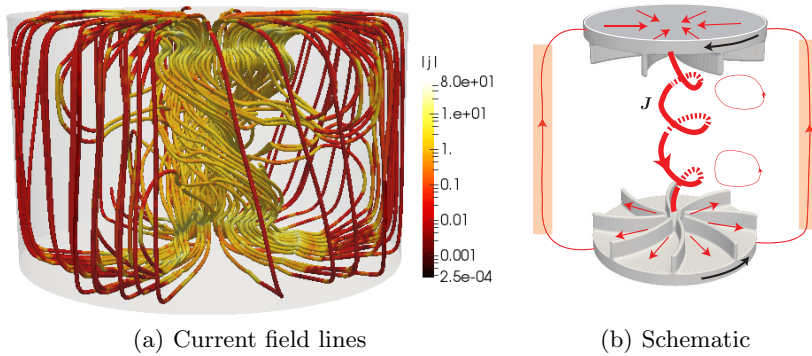


FIGURE 21. Current streamlines colored by the magnitude of  $\|\vec{j}\|$  and schematic of the dominant current field lines giving rise to the predominant axisymmetric time-averaged magnetic field of figure 18.

632 served at much higher Reynolds numbers (compare fig. 17(b) and fig.18(b) with fig. 6(b)  
 633 in Boisson et al. (2012)).

634 (c) Using ferromagnetic boundary conditions and  $\mu_r^{\text{imp}} = 50$ , we have found that the  
 635 critical magnetic Reynolds number scales like  $R_m^c - R_{m\infty}^c \approx 4100/R_e^{0.7}$  with  $R_{m\infty}^c = 68.8$ .  
 636 This value is in the range  $46 \leq R_m^c \leq 74$  where dynamo action has been observed in the  
 637 VKS2 setup (see Table I in Miralles et al. (2013)). This scaling suggests that the small

638 scales of turbulence do not seem to intervene in the dynamo mechanism at high  $R_e$   
639 numbers. The behavior of  $R_m^c$  with respect to  $R_e$  that we observed is somewhat at odd  
640 with other computations using simplistic forcings like Iskakov et al. (2007); Ponty et al.  
641 (2007); Reuter et al. (2011); Ponty and Plunian (2011). In all these simulations the  
642 critical magnetic Reynolds number has a non monotonic behavior with respect to  $R_e$ . It  
643 first increases with  $R_e$ , then either reaches a plateau or decreases after some intermediate  
644 value of  $R_e$  in the range [200, 1500]. Finally, it is suggested in Ponty and Plunian (2011)  
645 that “it is the mean flow which plays the most important role in the field generation even  
646 though it is 40% less intense than the fluctuations”. As shown in figure 9, the azimuthal  
647 Fourier modes  $m \in \{0, 3\}$  of the velocity contain most of the total kinetic energy at all the  
648 kinetic Reynolds numbers we have explored (the smallest being  $R_e = 500$ ). For instance  
649 these two modes contain about 75% of the total kinetic energy at  $R_e = 10^5$ . However  
650 the kinematic computations of section 5.1 have proved that the mean flow (averaged in  
651 time but not in space, therefore with non-axisymmetric features) gives a dynamo with  
652 a magnetic field mainly supported by the Fourier mode  $m = 1$  as already reported in  
653 the literature by us and others using an experimental time and azimuthally averaged  
654 velocity field. Therefore the VKS2 dynamo cannot be attributed to the mean flow. This  
655 argument shows that the disks play a major role.

656 To conclude, our simulations at high  $R_e$  numbers confirm that the ferromagnetic im-  
657 pellers are crucial to reduce the dynamo threshold and to obtain the predominantly  
658 axisymmetric dynamo mode observed in the VKS2 experimental setup. Looking at Fig-  
659 ure 21, where a schematic representation of the path followed by the electrical current is  
660 shown, let us imagine a vertical magnetic seed pointing upwards near one rotating im-  
661 peller. By  $\Omega$ -effect, the differential rotation of the impeller generates a toroidal magnetic  
662 field nearby the disk. This toroidal field is associated with a radial current ( $j_r \approx -\partial_z H_\theta$ )  
663 flowing outward in the bottom impeller and inward in the top one. The current circulates  
664 from the bottom impeller to the top one through a large scale loop inside the copper  
665 wall. Near the axis of the vessel the current flows downwards and the current lines are  
666 twisted by the flow in a way that regenerates the initial vertical field. This is the Bullard  
667 dynamo loop (Bullard (1955)) with the  $\Omega$ -effect due to the disks and the twisting-effect  
668 due to the flow.

## 669 Acknowledgments

670 The HPC resources for SFEMaNS were provided by GENCI-IDRIS (grant 2016-0254)  
671 in France and by the Texas A&M University Brazos HPC cluster. J.-L. Guermond ac-  
672 knowledges support from University Paris Sud, the National Science Foundation under  
673 grants DMS 1620058, DMS 1619892, the Air Force Office of Scientific Research, USAF,  
674 under grant/contract number FA99550-12-0358 and the Army Research Office, under  
675 grant number W911NF-15-1-0517. D. Castanon Quiroz acknowledges support by the  
676 Basque Government through ELKARTEK and the BERC 2014-2017 programmes and  
677 by Spanish Ministry of Economy and Competitiveness MINECO: BCAM Severo Ochoa  
678 excellence accreditation SEV-2013- 0323. L. Cappanera is thankful to Texas A&M Uni-  
679 versity, LIMSI, and CNRS for their financial support. W. Herreman at LIMSI is greatly  
680 acknowledged for fruitful discussions and drawing figures 1 and 21b.

## REFERENCES

- 681 S. Balay, S. Abhyankar, M. F. Adams, J. Brown, P. Brune, K. Buschelman, V. Eijkhout, W. D.  
682 Gropp, D. Kaushik, M. G. Knepley, L. C. McInnes, K. Rupp, B. F. Smith, and H. Zhang.

- 683 PETSc users manual. Technical Report ANL-95/11 - Revision 3.5, Argonne National Lab-  
 684 oratory, 2014.
- 685 J. Boisson and B. Dubrulle. Three-dimensional magnetic field reconstruction in the vks experi-  
 686 ment through galerkin transforms. *New Journal of Physics*, 13(2):023037, 2011.
- 687 J. Boisson, S. Aumaitre, N. Bonnefoy, M. Bourgoïn, F. Daviaud, B. Dubrulle, P. Odier, J.-F.  
 688 Pinton, N. Plihon, and G. Verhille. Symmetry and couplings in stationary von Kármán  
 689 sodium dynamos. *New Journal of Physics*, 14(1):013044, 2012.
- 690 A. Bonito and J.-L. Guermond. Approximation of the eigenvalue problem for the time harmonic  
 691 Maxwell system by continuous Lagrange finite elements. *Math. Comp.*, 80(276):1887–1910,  
 692 2011.
- 693 A. Bonito, J.-L. Guermond, and F. Luddens. Regularity of the Maxwell equations in heteroge-  
 694 neous media and Lipschitz domains. *Journal of Mathematical Analysis and applications*,  
 695 408(2):498–512, Dec. 2013.
- 696 E. C. Bullard. The stability of a homopolar dynamo. *Proc. Camb. Phil. Soc.*, 51:744–760, 1955.
- 697 D. Castanon Quiroz. *Solution of the MHD equations in the presence of non-axisymmetric con-*  
 698 *ductors using the Fourier-finite element method.* PhD thesis, Texas A&M College Station,  
 699 2015.
- 700 S. A. Colgate, H. Beckley, J. Si, J. Martinic, D. Westpfahl, J. Slutz, C. Westrom, B. Klein,  
 701 P. Schendel, C. Scharle, T. McKinney, R. Ginanni, I. Bentley, T. Mickey, R. Ferrel, H. Li,  
 702 V. Pariev, and J. Finn. High magnetic shear gain in a liquid sodium stable couette flow  
 703 experiment: A prelude to an  $\alpha - \Omega$  dynamo. *Phys. Rev. Lett.*, 106:175003, Apr 2011.
- 704 P.-P. Cortet, P. Diribarne, R. Monchaux, A. Chiffaudel, F. Daviaud, and B. Dubrulle. Nor-  
 705 malized kinetic energy as a hydrodynamical global quantity for inhomogeneous anisotropic  
 706 turbulence. *Physics of Fluids*, 21(2):025104, 2009.
- 707 P. Frick, V. Noskov, S. Denisov, and R. Stepanov. Direct measurement of effective magnetic  
 708 diffusivity in turbulent flow of liquid sodium. *Phys. Rev. Lett.*, 105:184502, Oct 2010.
- 709 U. Frisch. *Turbulence: the legacy of AN Kolmogorov.* Cambridge university press, 1995.
- 710 A. Gailitis, O. Lielausis, S. Dement’ev, E. Platācis, and A. Ciferons. Detection of a flow induced  
 711 magnetic field eigenmode in the Riga dynamo facility. *Phys. Rev. Lett.*, 84:4365, 2000.
- 712 A. Gailitis, O. Lielausis, E. Platācis, G. Gerbeth, and F. Stefani. The riga dynamo experiment.  
 713 *Surveys in Geophysics*, 24(3):247–267, 2003.
- 714 A. Giesecke, C. Nore, F. Stefani, G. Gerbeth, J. Léorat, F. Luddens, and J.-L. Guermond.  
 715 Electromagnetic induction in non-uniform domains. *Geophys. Astrophys. Fluid Dyn.*, 104  
 716 (5):505–529, 2010.
- 717 A. Giesecke, F. Stefani, and G. Gerbeth. Role of soft-iron impellers on the mode selection in  
 718 the von Kármán–sodium dynamo experiment. *Phys. Rev. Lett.*, 104(4):044503, Jan 2010.
- 719 A. Giesecke, C. Nore, F. Stefani, G. Gerbeth, J. Léorat, W. Herreman, F. Luddens, and J.-L.  
 720 Guermond. Influence of high-permeability discs in an axisymmetric model of the Cadarache  
 721 dynamo experiment. *New Journal of Physics*, 14(5):053005, 2012.
- 722 C. Gissinger. A numerical model of the VKS experiment. *Europhys. Lett.*, 87:39002–+, Aug.  
 723 2009. .
- 724 C. Gissinger, A. Isakov, S. Fauve, and E. Dormy. Effect of magnetic boundary conditions on  
 725 the dynamo threshold of von Kármán swirling flows. *EPL*, 82:29001, 2008.
- 726 J.-L. Guermond and J. Shen. On the error estimates for the rotational pressure-correction  
 727 projection methods. *Math. Comp.*, 73(248):1719–1737 (electronic), 2004. ISSN 0025-5718.
- 728 J.-L. Guermond, R. Laguerre, J. Léorat, and N. C. An interior penalty Galerkin method for the  
 729 MHD equations in heterogeneous domains. *J. Comput. Phys.*, 221(1):349–369, 2007.
- 730 J.-L. Guermond, R. Laguerre, J. Léorat, and C. Nore. Nonlinear magnetohydrodynamics in ax-  
 731 isymmetric heterogeneous domains using a Fourier/finite element technique and an interior  
 732 penalty method. *J. Comput. Phys.*, 228:2739–2757, 2009.
- 733 J.-L. Guermond, J. Léorat, F. Luddens, C. Nore, and A. Ribeiro. Effects of discontinuous  
 734 magnetic permeability on magnetodynamic problems. *J. Comput. Phys.*, 230:6299–6319,  
 735 2011a.
- 736 J.-L. Guermond, R. Pasquetti, and B. Popov. Entropy viscosity method for nonlinear conserva-  
 737 tion laws. *J. Comput. Phys.*, 230(11):4248–4267, 2011b.
- 738 J.-L. Guermond, R. Pasquetti, and B. Popov. From suitable weak solutions to entropy viscosity.  
 739 *Journal of Scientific Computing*, 49(1):35–50, 2011c.

- 740 J. Herault and F. Pétrélis. Optimum reduction of the dynamo threshold by a ferromagnetic  
741 layer located in the flow. *Physical Review E*, 90(3):033015, 2014.
- 742 E. Herbert, P.-P. Cortet, F. Daviaud, and B. Dubrulle. Eckhaus-like instability of large scale  
743 coherent structures in a fully turbulent von Kármán flow. *Physics of Fluids*, 26(1), 2014.
- 744 A. B. Iskakov, A. A. Schekochihin, S. C. Cowley, J. C. McWilliams, and M. R. E. Proctor.  
745 Numerical demonstration of fluctuation dynamo at low magnetic Prandtl numbers. *Phys.*  
746 *Rev. Lett.*, 98:208501, 2007. .
- 747 G. Karypis and V. Kumar. A fast and high quality multilevel scheme for partitioning irregular  
748 graphs. *SIAM Journal on Scientific Computing*, 20(1):359–392, 1998.
- 749 S. Kreuzahler, D. Schulz, H. Homann, Y. Ponty, and R. Grauer. Numerical study of impeller-  
750 driven von Kármán flows via a volume penalization method. *New Journal of Physics*, 16  
751 (10):103001, 2014.
- 752 R. Laguerre, C. Nore, J. Léorat, and J.-L. Guermond. Effects of conductivity jumps in the  
753 envelope of a kinematic dynamo flow. *CR Mécanique*, 334:593, 2006.
- 754 R. Laguerre, C. Nore, A. Ribeiro, J. Léorat, J.-L. Guermond, and F. Plunian. Impact of impellers  
755 on the axisymmetric magnetic mode in the VKS2 dynamo experiment. *Phys. Rev. Lett.*,  
756 101(10):104501, 2008.
- 757 L. Marié, C. Normand, and F. Daviaud. Galerkin analysis of kinematic dynamos in the von  
758 Kármán geometry. *Phys. Fluids*, 18:017102, 2006.
- 759 S. Miralles, N. Bonnefoy, M. Bourgoïn, P. Odier, J.-F. Pinton, N. Plihon, G. Verhille, J. Boisson,  
760 F. Daviaud, and B. Dubrulle. Dynamo threshold detection in the von Kármán sodium  
761 experiment. *Phys. Rev. E*, 88:013002, Jul 2013.
- 762 S. Miralles, N. Plihon, and J.-F. Pinton. Lorentz force effects in the Bullard-von Kármán  
763 dynamo: saturation, energy balance and subcriticality. *Journal of Fluid Mechanics*, 775:  
764 501523, 2015.
- 765 H. Moffatt. *Magnetic Field Generation in Electrically Conducting Fluids*. Cambridge Mono-  
766 graphs on Mechanics and Applied Mathematics. Cambridge University Press, Cambridge,  
767 UK, 1978.
- 768 R. Monchaux, M. Berhanu, M. Bourgoïn, P. Odier, M. Moulin, J.-F. Pinton, R. Volk, S. Fauve,  
769 N. Mordant, F. Pétrélis, A. Chiffaudel, F. Daviaud, B. Dubrulle, C. Gasquet, L. Marié,  
770 and F. Ravelet. Generation of magnetic field by a turbulent flow of liquid sodium. *Phys.*  
771 *Rev. Lett.*, 98:044502, 2007.
- 772 U. Müller, R. Stieglitz, and S. Horanyi. A two-scale hydromagnetic dynamo experiment. *Journal*  
773 *of Fluid Mechanics*, 498:3171, 2004. .
- 774 C. Nore, L. S. Tuckerman, O. Daube, and S. Xin. The 1:2 mode interaction in exactly counter-  
775 rotating von Kármán swirling flow. *Journal of Fluid Mechanics*, 477:51–88, 2 2003.
- 776 C. Nore, J. Léorat, J.-L. Guermond, and A. Giesecke. Mean-field model of the von Kármán  
777 sodium dynamo experiment using soft iron impellers. *Phys. Rev. E*, 91:013008, 2015.
- 778 C. Nore, H. Zaidi, F. Bouillault, A. Bossavit, and J.-L. Guermond. Approximation of the  
779 time-dependent induction equation with advection using whitney elements: Application to  
780 dynamo action. *COMPEL - The international journal for computation and mathematics*  
781 *in electrical and electronic engineering*, 35(1):326–338, 2016.
- 782 Nore, C., Castanon Quiroz, D., Cappanera, L., and Guermond, J.-L. Direct numerical simulation  
783 of the axial dipolar dynamo in the von krmn sodium experiment. *EPL*, 114(6):65002, 2016.
- 784 M. D. Nornberg, E. J. Spence, R. D. Kendrick, C. M. Jacobson, and C. B. Forest. Measurements  
785 of the magnetic field induced by a turbulent flow of liquid metal. *Physics of Plasmas*, 13  
786 (5):055901, 2006.
- 787 R. Pasquetti, R. Bwemba, and L. Cousin. A pseudo-penalization method for high Reynolds  
788 number unsteady flows. *Appl. Numer. Math.*, 58(7):946–954, July 2008.
- 789 N. L. Peffley, A. B. Cawthorne, and D. P. Lathrop. Toward a self-generating magnetic dynamo:  
790 The role of turbulence. *Phys. Rev. E*, 61:5287–5294, May 2000.
- 791 F. Pétrélis, N. Mordant, and S. Fauve. On the magnetic fields generated by experimental  
792 dynamos. *Geophys. Astrophys. Fluid Dyn.*, 101:289, 2007.
- 793 Y. Ponty and F. Plunian. Transition from large-scale to small-scale dynamo. *Phys. Rev. Lett.*,  
794 106:154502, 2011.
- 795 Y. Ponty, P. Mininni, J.-F. Pinton, H. Politano, and A. Pouquet. Dynamo action at low magnetic  
796 Prandtl numbers: mean flow vs. fully turbulent motion. *New J. Phys.*, 9:296, 2007.

- 797 F. Ravelet. *Bifurcations globales hydrodynamiques et magnétohydrodynamiques dans un*  
 798 *écoulement de von Kármán turbulent*. PhD thesis, Ecole Polytechnique X, 2005.
- 799 F. Ravelet, A. Chiffaudel, F. Daviaud, and J. Léorat. Towards an experimental von Kármán  
 800 dynamo : numerical studies for an optimized design. *Phys. Fluids*, 17:117104, 2005.
- 801 F. Ravelet, A. Chiffaudel, and F. Daviaud. Supercritical transition to turbulence in an inertially  
 802 driven von Kármán closed flow. *Journal of Fluid Mechanics*, 601:339–364, 2008.
- 803 F. Ravelet, B. Dubrulle, F. Daviaud, and P.-A. Ratié. Kinematic alpha tensors and dynamo  
 804 mechanisms in a von Kármán swirling flow. *Phys. Rev. Lett.*, 109:024503, Jul 2012.
- 805 K. Reuter, F. Jenko, and C. B. Forest. Turbulent magnetohydrodynamic dynamo action in a  
 806 spherically bounded von kármán flow at small magnetic prandtl numbers. *New Journal of*  
 807 *Physics*, 13(7):073019, 2011.
- 808 D. R. Sisan, W. L. Shew, and D. P. Lathrop. Lorentz force effects in magneto-turbulence. *Physics*  
 809 *of the Earth and Planetary Interiors*, 135(23):137 – 159, 2003. Magnetic Field Modelling.
- 810 R. Stieglitz and U. Müller. Experimental demonstration of a homogeneous two-scale dynamo.  
 811 *Phys. Fluids*, 13:561, 2001.
- 812 J. Varela, S. Brun, B. Dubrulle, and C. Nore. Role of boundary conditions in helicoidal flow  
 813 collimation: Consequences for the von kármán sodium dynamo experiment. *Phys. Rev. E*,  
 814 92:063015, Dec 2015.
- 815 G. Verhille, N. Plihon, M. Bourgoïn, P. Odier, and J.-F. Pinton. Induction in a von Kármán  
 816 flow driven by ferromagnetic impellers. *New Journal of Physics*, 12(3):033006, 2010.